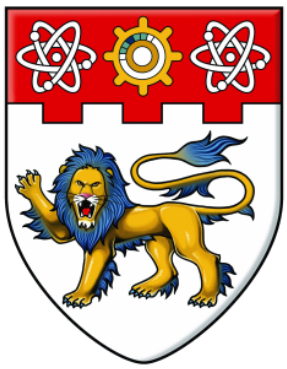

NANYANG TECHNOLOGICAL UNIVERSITY

# PHASE-CONTROLLED SYNTHESIS for 1T' PHASE $MoS_2$ and $MoSe_2$ CRYSTALS


**NAM GWANG-HYEON**

**INTERDISCIPLINARY GRADUATE SCHOOL**

**NTU Institute for Health Technologies (HealthTech NTU)**


**2018**

# PHASE-CONTROLLED SYNTHESIS for 1T' PHASE $MoS_2$ and $MoSe_2$ CRYSTALS

NAM GWANG-HYEON

Interdisciplinary Graduate School
NTU Institute for Health Technologies
(HealthTech NTU, MSE/EEE)

A thesis submitted to the Nanyang Technological University in partial fulfilment of the requirement for the degree of
Doctor of Philosophy

**2018**

# Statement of Originality

I hereby certify that the work embodied in this thesis is the result of original research and has not been submitted for a higher degree to any other University or Institution.

. . . . . .  . . . . . .

Date  Student Name

## Abstract

Polymorphism, existence of multiple forms of crystalline substances, has attracted research interest in transition metal dichalcogenides (TMDs) due to its drastic change of properties based on the crystallinity (phase). For example, $MoS_2$ is thermodynamically stable as a trigonal prismatic (2H phase, a semiconducting material) in ambient condition, but it can be metallic when it is octahedral (1T phase). However, it is hard to synthesize the 1T phase of $MX_2$ (M=Mo, W; X=S, Se) because they are metastable in ambient condition. To further study on phase-dependent properties, it is necessary to develop a facile method for phase-controlled synthesis. In this thesis, I describe research findings in two chapters.

First, I report phase-controlled synthesis method for 1T'-$MoX_2$ (X=S, Se) crystals with lateral size up to hundreds of micrometers. The 1T' phase structure was carefully characterized by various techniques including the aberration-corrected scanning transmission electron microscopy (STEM), X-ray photoelectron spectroscopy (XPS), X-ray absorption fine structure (XAFS) and Raman spectroscopy. By using metastable condition of the 1T' phase in $MoS_2$, the phase transition was achieved by thermal annealing and laser irradiation. In the end, phase-dependent electrochemical property for HER is demonstrated on the basal plane of $MoS_2$.

Second, I used the metallic $MoS_2$ to fabricate the tactile sensor to detect touch and press. The metallic $MoS_2$ nanosheets were prepared by Li intercalation method and integrated into a thin film by the vacuum filtration method. The film exhibited electrically conductive property and response from a touch of fingertips. The results offer the insight for development of a cost-effective tactile sensor.

# Authorship Attribution Statement

This thesis contains material from 37-62 paper(s) published in the following peer-reviewed journal(s) where I was the first and/or corresponding author.

Chapter 4 is published as **Yifu Yu, Gwang-Hyeon Nam, Qiyuan He, Xue-Jun Wu**, Kang Zhang, Zhenzhong Yang, Junze Chen, Qinglang Ma, Meiting Zhao, Zhengqing Liu, Fei-Rong Ran, Xingzhi Wang, Hai Li, Xiao Huang, Bing Li, Qihua Xiong, Qing Zhang, Zheng Liu, Lin Gu, Yonghua Du, Wei Huang & Hua Zhang. High phase-purity 1T′ -MoS2- and 1T′ -MoSe2-layered crystals. *Nature Chemistry,* **10**, 638–643 (2018). DOI: 10.1038/s41557-018-0035-6

The contributions of the co-authors are as follows:

- H.Z. proposed the research direction and guided the project.
- Y.Y., G.-H.N., Q.H. and X.-J.W. conceived the idea, designed the experiments and drafted the manuscript with H.Z., synthesized the materials, fabricated the devices, and analysed the data.
- K.Z. and Q.Z. helped with Raman and photoluminescence mapping measurements.
- X.W. and Q.X. conducted the temperature-dependent electrical property measurements.
- Z.Y. and L.G. carried out the STEM characterization.
- J.C., Q.M., M.Z. and Z.L. helped draft the manuscript.
- B.L. carried out XPS characterization.
- F.-R.R. and H.L. carried out AFM characterization.
- Y.D. analysed the XAFS results. Z.L., X.H. and W.H. helped revise the manuscript.

. . . . . . . . . . . . . . . . . .                . . . . . . . . . . . . . . . . . . . . . . . . . . . . .

Date

## Acknowledgements

First and foremost, I am particularly grateful to my supervisor, Professor Hua Zhang, for his inspiring guidance and encouragement through my entire PhD candidate.

I would like to thank my co-supervisor, Prof. Qing Zhang, and mentor, Dr. Hong Liang Tey for their valuable advice and support to my research work.

I appreciate the help from group members and friends: Dr. Yifu Yu, Dr. Qiyuan He, Dr. Xuejun Wu, Dr. Junze Chen, Dr. Qipeng Lu, Dr. Xiao Zhang, Dr. Qinglang Ma, Dr. Meiting Zhao, Dr. Apoorva Chaturvedi, Dr. Xiehong Cao, Prof. Hai Li, Dr. Zhimin Luo, Dr. Shikui Han, Dr. Zhanxi Fan, Dr. Chaoliang Tan, Dr. Jian Yang, Dr. Bo Chen, Dr. Zhicheng Zhang, Mr. Zhuangchai Lai, Dr. Ying Huang, Dr. Jumiati Wu, Mr. Dianyi, Ms. Ye Chen, Ms. Jiawei Liu, Dr. Zhang Kang, Dr. Xingzhi Wang, and all other colleagues.
The support from the technicians of the laboratories is also appreciated.
This thesis is dedicated to my family. Thank my father, Mr. Mun-Hee Nam and mother, Mrs. Sueng-Sun Lee. Thank my sister, too. Thank my wife, Dr. Jieun Ko for supporting my life.

# Table of Contents

## Table Captions

# Figure Captions

# Abbreviations

1D One-dimensional

2D Two-dimensional

AFM Atomic Force Microscopy

CB Conduction Band

CVD Chemical Vapor Deposition

DOS Density of States

EDS Energy Dispersive X-ray Spectroscopy

FET Field-effect Transistor

$H_2O$ Water

HER Hydrogen Evolution Reaction

HR-TEM High-resolution Transmission Electron Microscopy

Li Lithium

$MoS_2$ Molybdenum Disulfide

$MoSe_2$ Molybdenum Diselenide

$N_2$ Nitrogen

PL Photoluminescence

SAED Selected Area Electron Diffraction

SEM Scanning Electron Microscopy

STEM Scanning Transmission Electron Microscopy

TMD Transition Metal Dichalcogenide

TEM Transmission Electron Microscopy

VB Valence Band

$WS_2$ Tungsten Disulfide

XRD X-ray Diffraction

XPS X-ray Photoelectron Spectroscopy

# Chapter 1

# Introduction

*This chapter is for a brief introduction of the thesis. First, hypothesis/problem statement of the thesis is described. The objectives and scope is proposed based on the hypothesis/problem statement. After that, the dissertation overview for each chapter is presented, and then finally, the findings and outcomes are summarized.*

## 1.1 Hypothesis/Problem Statement

Fossil fuels are still our major source of energy supply, but importance for developing sustainable energy technologies keeps increasing due to several concerns such as resource depletion and carbon dioxide emission. Renewable energy has become one of the most important research topics in current scientific and industrial communities. Electrochemical water splitting, producing hydrogen and oxygen, is one of the promising candidates of renewable energy, however still far from economically feasible due to its dependence on noble-metal electrocatalyst such as platinum[1, 2]. Therefore, it is crucial to develop economically viable electrochemical catalysts with high activity.

Transition metal dichalcogenides (TMDs) are among the most encouraging candidates for electrocatalytic hydrogen evolution reaction (HER) in the non-noble metal based catalysts[3]. Previous studies have found that introducing metallic phase by chemical or electrochemical methods into $MoS_2$ and $WS_2$ (the semiconducting TMDs) dramatically enhanced the electrocatalytic performance[4]. However, it is currently unclear whether the crystal phase or other effects such as active sites and conductivity plays the critical role. For example, controlled-phase synthesis is of importance in the inorganic materials because the different phase influence on intrinsic physical and chemical properties such as electrical conductivity and chemical reactivity[5, 6]. It is therefore desirable to realize phase-controlled synthesis of TMDs with high purity. Material preparation with phase-control has been in demand for group VI transition metal dichalcogenides with the metallic-phase. Several approaches have been reported to prepare metallic-phase group VI TMDs, but those results were suffered from the poor purity and stability, because the 1T/1T' phase of $MoS_2$ and $MoSe_2$ are easily changed to the 2H phase due to its metastable feature. Hence, it is of importance to establish a universal method for producing

metallic (1T') phase $MX_2$ (M=Mo, W; X=S, Se) crystals and study their crystal phase-dependent properties and HER performance.

## 1.2 Objectives and Scope

Group VI transition metal dichalcogenides (TMDs) have intrigued research interest as a result of extraordinary properties in mechanical, optical and electrical properties derived from their layered and atomically thin structures[7]. One of promising application for TMDs is the hydrogen evolution reaction to replace noble metal catalysts such as Pt and Ru which are expensive[8]. Even though $MoS_2$ has been studied as electrocatalyst for HER, it has been suffered from its intrinsic electrical property which is semiconducting materials causing high internal resistivity. Notably, the electrical property of TMDs is dramatically changed by its crystal phase, i. e. trigonal prismatic (2H) and octahedral (1T)[9, 10]. In 1T phase, the $MoS_2$ exhibits metallic property which is more applicable for HER than semiconducting property. Several methods have been developed to achieve the metallic phase $MoS_2$ by alkali metal intercalation[11, 12], e-beam irradiation[13] but the results from those methods were insufficient to clarify the intrinsic properties and influence to HER performance. Therefore, it is of great fundamental interest to develop an approach for producing bulk metallic-phase TMDs crystals and further revealing their properties depending on phases and application.
Based on the aforementioned problem statement, the objective and scopes of this thesis are below:

First, it is described for a method to synthesize the phase-controlled 1T'-$MoS_2$ and 1T'-$MoSe_2$ crystals by flux method. The crystals were investigated by various methods such as aberration-corrected scanning transmission electron microscopy (STEM), X-ray absorption fine structure (XAFS), X-ray photoelectron spectroscopy (XPS), and Raman spectroscopy. The phase

transformation was achieved from 1T'-$MoS_2$ to 2H-$MoS_2$ by using both heat treatment and laser irradiation. Three different kinds of microcells with 1T' phase or 2H phase $MoS_2$ were designed to clarify the factors for HER in $MoS_2$. In the end, the phase-dependent efficiency of basal plane in $MoS_2$ is demonstrated for the electrochemical hydrogen evolution reaction.

Second, I investigate on in-plane anisotropic optical and electrical properties of 1T'-$MoS_2$ nanosheet. The distorted octahedral structure is confirmed by the high-resolution transmission electron microscopy (HR-TEM) and aberration-corrected scanning transmission electron microscopy (STEM). Anisotropic lattice vibrations and electrical carrier transport are observed by angle-resolved Raman spectroscopy and electronic measurement, respectively.

## 1.3 Dissertation Overview

The thesis addresses the phase-controlled synthesis of Molybdenum-based TMDs via flux method. 1T' phase $MoS_2$ and $MoSe_2$ have been synthesized and characterized by various methods to confirm the quality of materials. Intrinsic properties were analyzed and, from the arrangement of Mo atoms, unique anisotropic properties were exhibited. Based on its thermodynamic stability, the concept of phase patterning was demonstrated. In the end, it is demonstrated for phase dependent activity of basal plane in 1T'-$MoS_2$ for HER.

*Chapter 1* provides a rationale for the research. At first, problem is stated and then, it is introduced for objective and scopes.

*Chapter 2* reviews the literature concerning recent progress in the TMD materials. Specifically, it is described on synthesis methods and intrinsic properties. Furthermore, the importance of phase control synthesis is covered.

*Chapter 3* discusses the principles underlying the phase-controlled synthesis and the methods for data analysis. In this chapter, it is explained about particular methods for analyzing results that confirm atomic structures as the phase designed in detail.

*Chapter 4* elaborates a facile method for the crystal phase-controlled synthesis of 1T'-$MoS_2$ and 1T'-$MoSe_2$ crystals. Additionally, the crystals are used to demonstrate phase transition and phase-dependent hydrogen evolution reaction.

*Chapter 5* elaborates on a skin-inspired $MoS_2$ touch sensor. The thin-film prepared by $MoS_2$ nanosheet solution are electrically conductive and the resistivity and transparency could be controlled by the amount of nanosheet solution.

*Chapter 6* conclude whole research in this thesis.

## 1.4 Findings and Outcomes/Originality

This research led to several novel outcomes by:

1. Establishing a new method to synthesize **bulk 1T'-$MoS_2$ crystals** with high purity. The pure crystals provide a good platform for exploring their properties, which is impossible to fulfill with previously reported mixture of metallic and semiconducting phase $MoS_2$ nanomaterials.

2. Correlating the **distorted octahedral coordinated structure** of 1T'-$MoS_2$ is studied by STEM, X-ray photoelectron spectroscopy (XPS), Raman and photoluminescence (PL) spectroscopy. Furthermore, the **intrinsic anisotropic optical and electrical property** of 1T'-$MoS_2$ crystals is revealed.

3. The laser-induced **phase transition process** from 1T'-$MoS_2$ to 2H-$MoS_2$

at desired position with a **controlled manner** is also verified.

4. The crystal phase-dependent electrocatalysis in TMDs is clarified. Our synthesized 1T'-$MoS_2$ crystals provide a unique opportunity to study crystal phase-dependent catalytic properties. By carefully designing the electrochemical microcells, it was able to exclude the effect of edges and isolate the electrochemical activities of the basal plane of 1T'-$MoS_2$.

5. $MoS_2$ thin-films prepared by nanosheet solution are electrically conductive and the resistivity and transparency could be controlled by the amount of nanosheet solution. The skin-inspired $MoS_2$ sensor distinguished a touch of bare fingertip, and the touch and pressure could be discriminated by the different pattern from electrical signals.

**References:**

[1] S. Licht, B. Cui, J. Stuart, B. Wang, J. Lau, *Energy Environ. Sci.* **2013**, 6, 3646−3657.

[2] N. S. Lewis, D. G. Nocera, *Proc. Natl. Acad. Sci. USA*. **2006**, 103, 15729−15735.

[3] Q. Lu, Y. Yu, Q. Ma, B. Chen, H. Zhang, *Adv. Mater.* **2016**, 28, 1917–1933.

[4] D. Voiry, *et al. Nano Lett.* **2013**, 13, 6222–6227.

[5] C. Thelander, P. Caroff, S. Plissard, A. W. Dey, and K. A. Dick. *Nano Lett.* **2011**, 11, 2424–2429.

[6] Z. Fan, *et al. J. Am. Chem. Soc.* **2016**, 138, 1414–1419.

[7] C. Tan, *et al. Chem. Rev.* **2017**, 117, 6225–6331.

[8] D. Voiry, J. Yang, M. Chhowalla, *Adv. Mater.* **2016**, 28, 6197.

[9] M. Chhowalla, *et al. Nat. Chem.* **2013**, 5, 263–275.

[10] M. A. Lukowski, *et al. J. Am. Chem. Soc.* **2013**, 135, 10274–10277.

[11] M. A. Py and R. R. Haering. *Can. J. Phys.* **1983**, 61, 76–84.

[12] Zeng, Z. *et al. Angew. Chem. Int. Ed.* **2011**, 50, 11093–11097.

[13] Y.-C. Lin, D. O. Dumcenco, Y.-S. Huang, and K. Suenaga. *Nat. Nanotech.* **2014**, 9, 391–396.

# Chapter 2

# Literature Review

*In this chapter, I provide the literature review on the recent progress for 2D TMD materials. First, compositions and crystal structures are depicted and then, the strategies for effective control of phases are reviewed with obstacles to be solved. Third, the application for phase-controlled materials are introduced including important role of phase control in this area. In the end, some tasks related to this thesis is addressed based on literature review.*

## 2.1 Overview

Research interest on two-dimensional (2D) layered materials has been widely promoted since graphene mechanically exfoliated was discovered[1]. 2D graphene has shown extraordinary properties distinguished from bulk graphite such as unique electronic band structure[2], superior carrier mobility[3] and molecular barrier property[4], providing researchers with new research area. For a decade, this discovery has led to tremendous development on methodology dealing with 2D materials, and the methodology has been embarked on applying to other 2D materials, especially transition metal dichalcogenides (TMDs). [5-7]

TMDs have also layered structure and properties dependent on thickness. In contrast to graphene, they show diverse electrical properties from metallic to dielectric as occupancy in d-orbitals of the transition metal[8]. Due to various properties, TMDs has been extensively researched in various area. In TMDs, molybdenum disulfide ($MoS_2$) has been researched thanks to its affordability as molybdenite. It was the progress dealing with 2D materials and availability of $MoS_2$ that were the basis for the explosive studies. Many research unveiled the properties of $MoS_2$. It has metallic and semiconducting properties based on its structure[9], and high mobility of more than 200 $cm^2V^{-1}S^{-1}$, on-off ratios of $10^8$ and low power consumption[10]. The exotic properties have been researched for electronics, catalysis, photovoltaics and batteries.

## 2.2 Composition and crystal structures of 2D transition metal dichalcogenides

TMDs usually are made up of one transition metal (M) and two chalcogenides (X) as a layered structure such as a graphene. A formula of the TMDs is $MX_2$ and an oxidation numbers of dichalcogenides and transition metal are -2 and +4, respectively[8]. In the case of $MoS_2$, it is a combination between the molybdenum of group 6 and the sulfur of group 16. Each layer is approximately from 6 to 7 Å in thickness, stacked vertically with hexagonally packed structures[10]. The molecular geometry of TMDs is able to either trigonal prismatic ($D_{3h}$) or octahedral ($D_{3d}$) and out of these geometry, trigonal prismatic is more stable for $MoS_2$ in theory[11]. This geometry is connected with in-plane covalent bonds, but in the case of out of plane, van der Waals force. Due to bonding energy difference between covalent bond and van der Waals force, layer separation is easy with a method using smaller energy such as mechanical exfoliation compared to breakdown of the layer. Furthermore, the structure of $MoS_2$ (S-Mo-S) typically leads to various polymorphs such as 1T, 2H, 3R (T: trigonal, H: hexagonal, R: rhombohedral) as shown in Fig. 2.2.1. Interestingly, these polymorphs reflect origin of its formation. For example, 1T phase is found in $MoS_2$ prepared via Li-intercalation method. 2H phase is generally exhibited in natural $MoS_2$ and 3R phase is discovered in synthetic $MoS_2$[12].

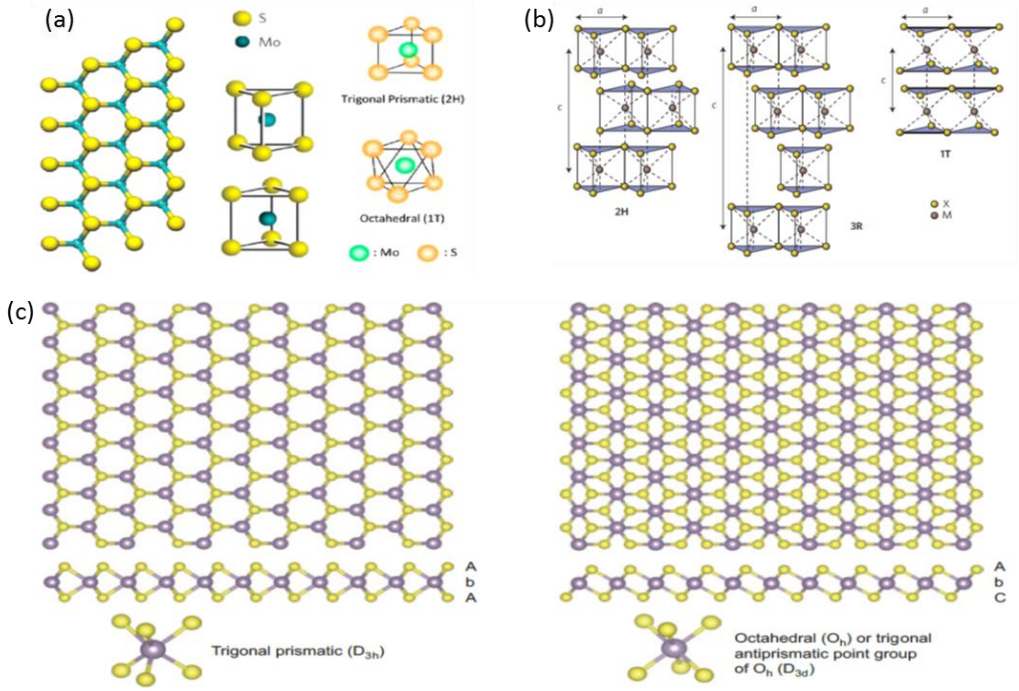


**Figure 2.2.1** Schematics of (a) crystal structure of $MoS_2$. (b) Structural polytypes: 2H (trigonal prismatic coordination, $D_{3h}$, hexagonal symmetry), 3R (trigonal prismatic coordination, $D_{3h}$, rhombohedral symmetry), 1T (octahedral coordination, $O_h$). (c) z-axis view of trigonal prismatic and octahedral coordination. [8]

## 2.3 Intrinsic properties of TMDs

### 2.3.1 Electrical and mechanical properties

The electronic structure of $MoS_2$ is mainly influenced from metal coordination and polymorphs which result in change of the number of d-electron. According to crystal field theory, the d-orbitals split into different orbitals in octahedral or trigonal prismatic complex, respectively. These orbitals from each complex have different energy levels, resulting in variation of electron capacity. Because the d-orbitals of 1T-$MoS_2$ is not filled completely, it can act as a metal. On the other hand, 2H-$MoS_2$ exhibits a semiconducting property due to fully filled $d_{z^2}$ orbitals. In contrast to the number of electrons in d-orbitals of the transition metal atom, a kind of chalcogenide atom is less effective for the electronic structure. But it is still important for fine tuning of band-gap because the band-

gap correspondingly decrease ranging from 1.3 to 1.0 eV when the size of chalcogenide atom increase from a sulfur to a tellurium[12].

The mechanical property of $MoS_2$ is commensurate to that of graphene. Monolayer $MoS_2$ has physical strength of 270 GPa in young's modulus, and it is even higher than the value of steel and tensile strength of 16-30 GPa[13]. These breaking strength are an area of theoretical upper limit, which indicates the $MoS_2$ layer is predominantly defect-free. Even though it is atomically thin, it has potential to use in diverse electronics due to the mechanical robustness and electrical properties.

### 2.3.2 Electronic band structure and optical properties

It is unique that the number of layers is significantly influenced for the electronic band structure of $MoS_2$. From the monolayer to bulk $MoS_2$, the band gap between the valence band maximum (VBM) and conduction band minimum (CBM) varies in range from 1.95 to 1.2 eV[14]. In the Fig. 2.3.1, the direct band gap is placed at K point whereas the CBM is located between K-Γ and VBM is positioned at Γ point which comprise in-direct band-gap. Arrestingly, both points of the indirect band gap move to opposite direction with decreasing the number of layers due to quantum confinement effect and change of orbital hybridization between p on sulfur and d on molybdenum atoms. Compared to the indirect band gap, the distance of direct band gap less influence to the thickness of layers via less dependence from aforementioned hybridization. Furthermore, the band gap property dependent on the layer thickness affects to the optical features of the material. For example, research has detected changes of absorption spectra, photoluminescence and photoconductivity with tendency on the thickness (Fig. 2.3.2)[15-17]. Quantum yield of monolayer $MoS_2$ is 4 orders higher than that of bulk, but there is still a problem to solve which is low value of quantum yield in a monolayer ($4 \times 10^{-3}$)[16]. In $MoS_2$, photoluminescence (PL) peak is mainly characterized as A and B excitons at K point. These peaks are tuned through applying excess

carriers[18] or mechanical strain[19]. In the former case, trions are generated via interactions among an excited electron-hole pair and a hole or electron. Trions typically are not stable in room temperature, but exceptionally the trions in $MoS_2$ can be observed at room temperature due to strong binding energy. In the latter case, in addition to change of PL peak positions, intensity of PL peaks is also changed because relaxation pathway is altered from direct to in-direct band-gap by strain-induced band-gap transformation. When the strain is applied to a bilayer $MoS_2$, the both band-gaps are simultaneously reduced at different rate of 67, 94 meV/% strain, respectively.

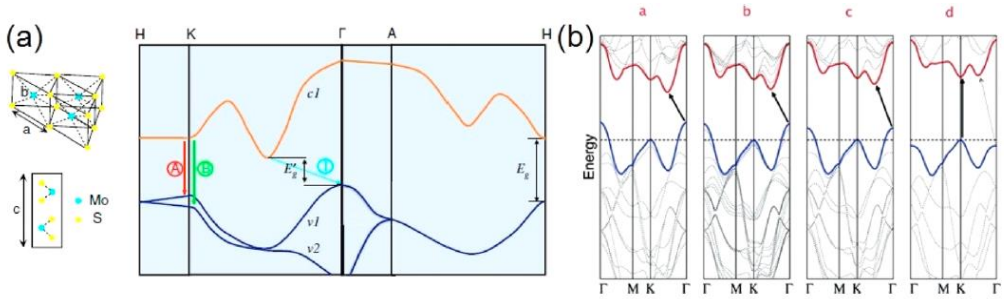


**Figure 2.3.1** (a) Simplified electronic band structure of bulk $MoS_2$, exhibiting split valence bands. Arrow A and B illustrate for direct band gap transitions whereas I shows an indirect band gap transition. (b) Change of electrnoic band strcuture of $MoS_2$ depending on the thickness[16].

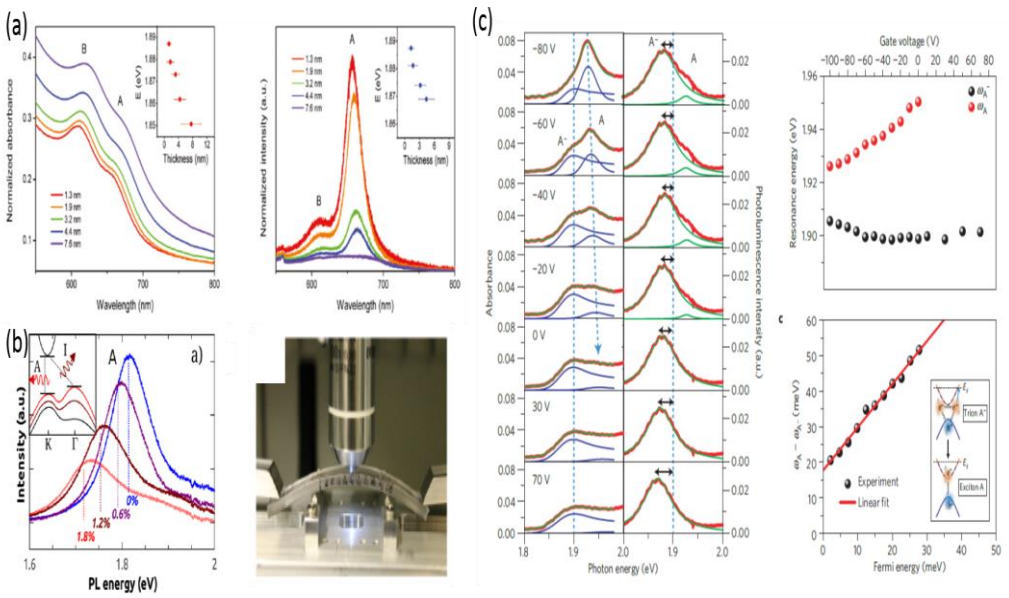


**Figure 2.3.2** (a) Absorption and photoluminescence spectra of $MoS_2$[17]. (b) Strain-engineering photoluminescence spectra[19]. (c) Trion behaviors of the optical properties of a monolayer $MoS_2$ from gate voltage dependence[18].

### 2.3.3 Lattice vibration properties

The lattice vibration properties of $MoS_2$ have widely been researched through Raman spectroscopy[20]. Main vibrations in $MoS_2$ are the $E^1_{2g}$ in-plane and $A^1_g$ out of plane mode (Fig. 2.3.3). The modes exhibit tendency with thickness of $MoS_2$. With decreasing the number of layers, the $E^1_{2g}$ mode (near 380 $cm^{-1}$) steadily increases while the $A^1_g$ modes (near 406 $cm^{-1}$) decreases, resulting that the gap distance between two modes become narrower. Therefore, Raman spectroscopy is powerful method to distinguish the layer thickness. The reason for the $E^1_{2g}$ shift is related to the dielectric screening effect of long-range coulomb interactions[21] whereas the $A^1_g$ shift is less affected by the interaction. Instead, the $A^1_g$ is susceptible to electron doping effect[22]. This unique property has led to the research area to pioneer the advanced sensing platform such as a molecule sensor[23].

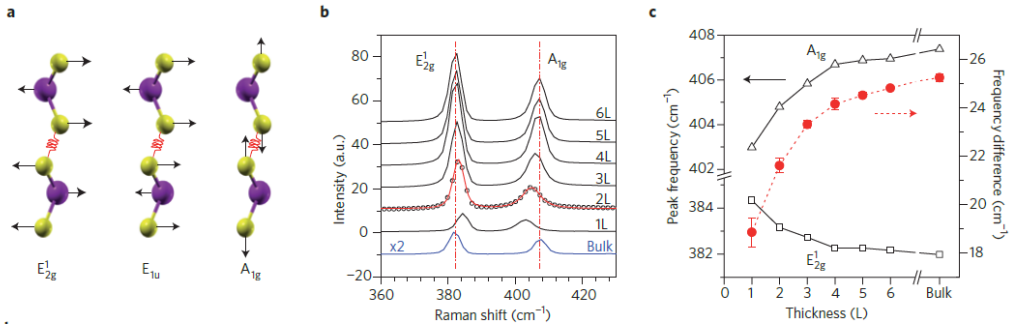


**Figure 2.3.3** (a) Schematics of $E^1_{2g}$, $E_{1u}$ and $A_{1g}$ phonon modes. (b) Thickness dependence of Raman spectra shift[21]. (c) Graph indicating Raman spectra shift for the peak position versus the thickness[20].

## 2.4 Preparation strategies of transition metal dichalcogenides

### 2.4.1 Fabrication of $MoS_2$ – Top-down

To prepare $MoS_2$ for various purposes, there are several approaches to fabricate the suitable $MoS_2$ (Fig. 2.4.1). First of all, mechanical exfoliation opened new era to investigate unique properties in $MoS_2$ using an adhesive tape[24]. Bulk $MoS_2$ can be exfoliated into even a monolayer thickness and the number of exfoliated nanosheets is rapidly measured by an optical microscopy (Fig. 2.4.1)[25]. The output from this method has single crystallinity and clean surface ideal for fundamental studies on characterization. However, mass production is still obstacle.

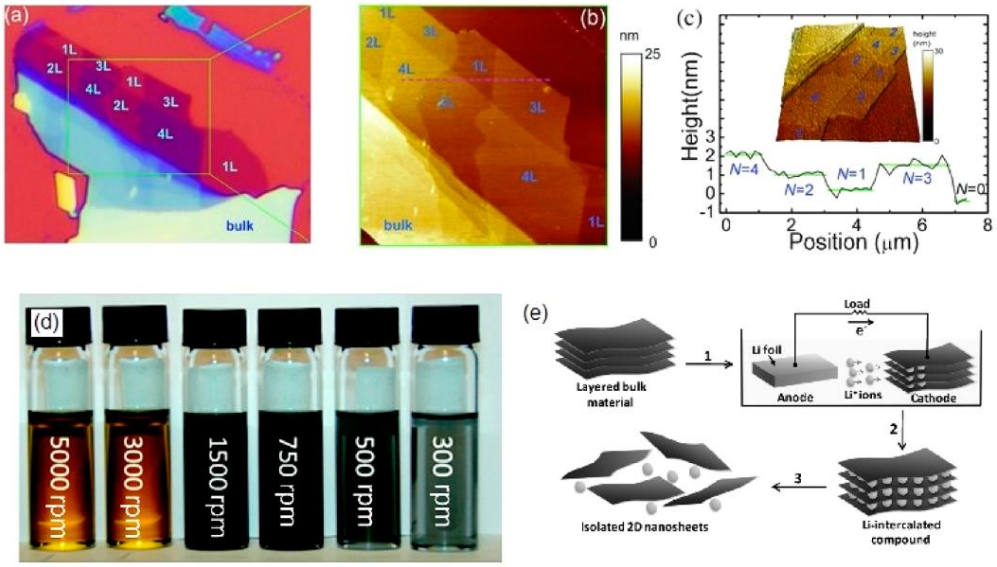


**Figure 2.4.1** Top-down fabrication. Multilayer $MoS_2$ characterization using the (a) optical (b, c) AFM spectroscopy[25]. (d) Liquid exfoliated $MoS_2$ by NMP as a solvent[26]. (e) Schematic of the Li-intercalated exfoliation method.

Liquid exfoliation is able to produce more amount of $MoS_2$. Various solvents such as N-methylpyrrolidone (NMP) and isopropyl alcohol (IPA) which can interact with $MoS_2$ surfaces are used for this method under sonication[26]. Water has also been used for exfoliation with diverse surfactants under sonication[27]. Intercalating molecules should compensate adhesion energy of inter-layer interactions[28] and the method exhibits lower effectiveness without sonication. But, sonication breaks $MoS_2$ nanosheets into sub-micron scales[29] and thus this method is applicable to research on catalysts, fillers. This method further improved in combination with a solvent, sonication time, centrifugation condition for separating the materials, resulting in concentration from 0.25 to 0.3 mg/ml[26].

Intercalation is promising separation strategy for high yield preparation. Especially, lithium intercalation reported in 1975[30]. At first, bulk specimen is immersed in a solution containing n-butyl lithium for a day. During the period, lithium ions penetrate into gaps between $MoS_2$ layers. The fully Li-intercalated

bulk specimens transfer to aqueous solution to generate the hydrogen, allowing them to separate each other. To overcome long experimental time, similar strategy was applied to electrochemical process by electrochemical method from our group[31]. Through the process, reaction time becomes much shorter (a few hours) and the amount of intercalation can be controlled. Distinctively, the $MoS_2$ prepared by intercalation method shows octahedral structure (1T-$MoS_2$) which has metallic property. The octahedral structure is transformed to trigonal prismatic structure by annealing at 300°C and band-gap structure is also restored[32].

### 2.4.2 Fabrication of $MoS_2$ – Bottom-up

Although primary studies have scrutinized using $MoS_2$ prepared by top-down method, it seems to need more time for top-down to break through the limitation for large-scale fabrication. For versatile availability in an industrial area, it is necessary to develop the process for large area with a uniform structure. The bottom-up synthesis may possible to lead to new era, resolving above-mentioned problems.

Chemical vapor deposition, or CVD, has been researched for the purpose to fabricate large-area synthesis of $MoS_2$ (Fig. 2.4.2)[33-35]. To explain these strategies, different precursors have been used for each CVD synthesis. Lee and co-workers deposited $MoS_2$ using $MoO_3$ and sulfur powders under co-vaporized condition. In this report, it was reported that aromatic molecules such as graphene oxide can assist growth of $MoS_2$ on substrates. Zhan and coworkers fabricated $MoS_2$ of approximately 1 $cm^{-2}$ from single-layer to 5 layers on the Mo metal thin film by the sulfurization[36], completing it in 5 h under 750 °C. Liu and co-workers[34] showed a two-step method via dip-coating and annealing process for large-area $MoS_2$ more than 3 $cm^{-2}$. For example, substrates such as a sapphire or $SiO_2$/Si wafer were cleaned and dipped into $(NH_4)_2MoS_4$ solution and then heated at 500 °C in $Ar/H_2$ condition to avoid oxidation, followed by

annealing them at 1000 °C in Ar/S gas to enhance the crystallinity. These approach overcame to synthesize sub-square centimeter area for $MoS_2$.

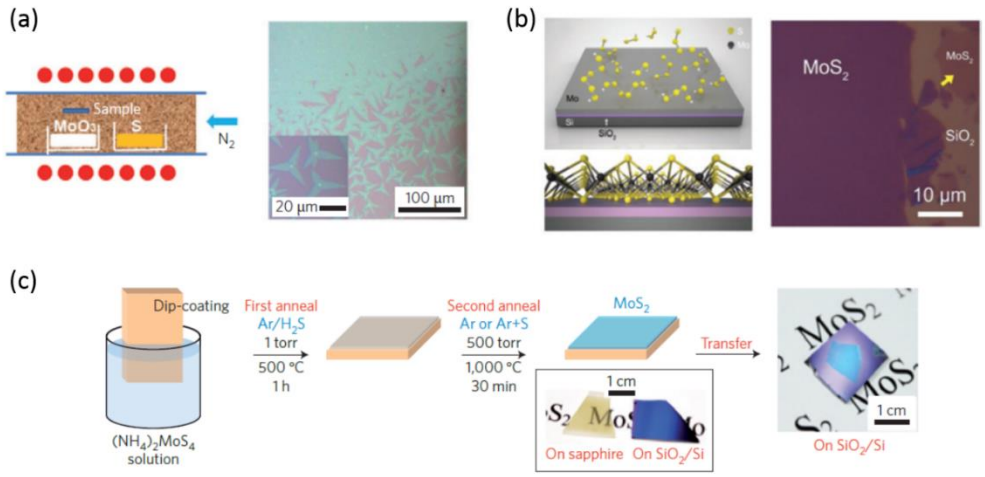


**Figure 2.4.2** Bottom-up fabrication. Schematic and an optical image of CVD of $MoS_2$ from (a) solid S and $MoO_3$ precursors[33]. (b) Sulfur exposure on the Mo substrate[36]. (c) $(NH_4)_2MoS_4$ using a dip-coating method[34].

### 2.4.3 Phase engineering in 2D transition metal dichalcogenides

Octahedral-structured TMDs, 1T-$MX_2$ (M = transition metals, X = chalcogen atoms), are composed of $MX_2$ layers derived from $MX_6$ octahedral structure. In the case of an undistorted structure, it has a hexagonal lattice which is observable from $TiS_2$ containing no electron in d orbital ($d^0$). Interestingly, the 1T-$MX_2$ phases show various lattice structures based on the numbers of electrons in d orbital of transition metals. For example, $TaS_2$, which has $d^1$ metal ion, exhibits periodic lattice distortions of metal atoms[37], and β-$MoTe_2$ and $WTe_2$, which has $d^2$ metal ion, consist of zigzag chain structure[38,39].
$MoS_2$, group VI TMDs with $d^2$ metal ion, has been observed trigonal prismatic structure (2H) in nature. However, the phase transition was induced in $MoS_2$ during Li intercalation for exfoliation[40]. The anomalous phenomenon has attracted research interest to establish the mechanism of phase transition. According to the crystal field theory, the $d_{z^2}$ orbital is the lower energy level in 2H phase while the $d_{xy,yz,zx}$ orbital is the higher energy level in 1T phase than that of the $d_{z^2}$ orbital. In the case of transition metals with $d^2$ state, 2H phase in $MoS_2$ is more thermodynamically stable than 1T phase in $MoS_2$ by filling two

electrons into the $d_{z^2}$ orbital which is the lowest energy level in the configuration[41]. However, as Li atoms are intercalated into 2H-$MoS_2$, some of electrons in Li transfer to the $MoS_2$. The excess electrons need to be filled into $d_{xy}$, $d_{x^2-y^2}$ orbitals in 2H phase, and the $d_{xy,yz,zx}$ orbital is more suitable to stabilize $MoS_2$ with excess electrons donated by Li atoms[42]. Therefore, phase transition can be considered as the stabilization process of the materials related to the number of electrons in d orbital of transition metals.

## 2.5 The application for TMDs

### 2.5.1 Hydrogen evolution reaction

Hydrogen is regarded as the environmentally friendly energy sources. To replace fossil fuels due to problems related to resource depletion and environmental pollution, the hydrogen production have the limelight. One of the general methods to produce hydrogen is water splitting which is the chemical reaction to decompose the water into oxygen and hydrogen. In this reaction, catalysts play an important role in the hydrogen evolution reaction (HER) process to achieve high productivity by reducing the overpotential and minimizing Gibbs free energy. Fig. 2.5.1 illustrates the HER activity of different catalysts, plotting the exchange current density ($i_0$) for hydrogen evolution versus the simulated Gibbs free energy for the absorbed hydrogen atom over diverse catalysts[43]. From the Fig. 2.5.1, we can see that Pt is located at top of the volcano curve. Commonly, catalysts for HER are efficient under acidic condition. But those efficient catalysts are expensive because they are mainly rare-earth metals. Therefore, the development of HER electrocatalysts with high efficient and low cost is of great important. $MoS_2$ is considered as the promising catalyst to replace Pt since it is close to the Pt group metals. Many experiments demonstrated that the edge of $MoS_2$ plays an important role for HER. Generally, it is simple for the process of the electron transfer in a single-layer $MoS_2$ nanosheet, which is from support to the nanosheet, while that for the electron transfer of $MoS_2$ nanoparticle is more complex, which is attributed to the additional process that the electrons need to pass through each layers[44],

increasing the resistance, as shown in Fig. 2.5.2. It can be seen that the $MoS_2$ nanosheet has a promising structure for HER, especially single-layer $MoS_2$ nanosheet.

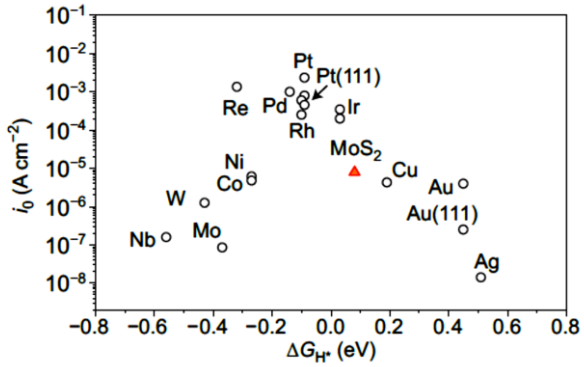


**Figure 2.5.1** A plot of the exchange current density ($i_0$) for hydrogen evolution versus the simulated Gibbs free energy for the absorbed hydrogen atom over various metals and $MoS_2$[43].

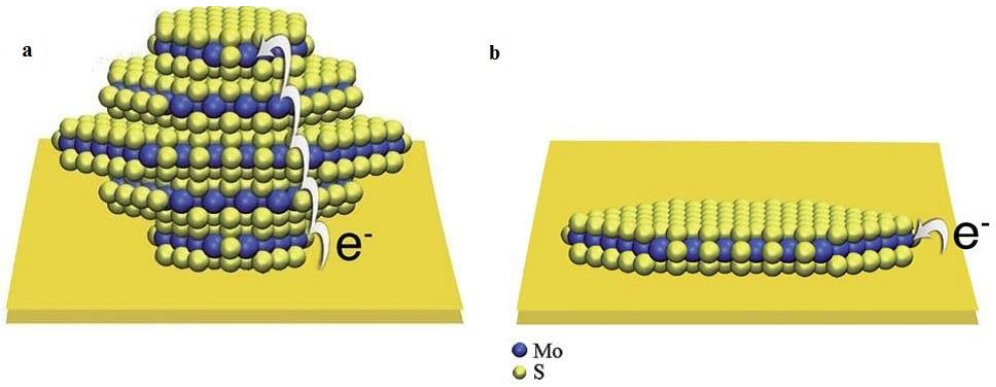


**Figure 2.5.2** Schematic of the conductivity of active sites on $MoS_2$ nanoparticle (a) and nanosheet (b) [44].

According to the aforementioned results, there has been tremendous research efforts for enhancing the HER performance of $MoS_2$ nanosheet to compete against rare-earth metals. The main approaches are to decrease the resistivity of $MoS_2$ nanosheet and to expose the more number of the HER active sites. For example, gold nanoparticle is decorated on the surface of $MoS_2$ nanosheet to reinforce the electron transfer and inhibit restacking nanosheets[45]. The number

of layers also influences to the catalytic performance in $MoS_2$ nanosheets. The catalytic activity of $MoS_2$ decreases with the addition of the each number of layer by a factor of 4.47 [46]. The results reveal that improving the efficiency of electron transfer toward the vertical direction is another efficient way to design $MoS_2$ with high catalytic activities. Accordingly, ultrathin $MoS_2$ nanosheet with many active sites may be a promising candidate for HER. The defect-rich $MoS_2$ ultrathin nanosheet (Fig. 2.5.3a) showed an HER activity with a Tafel slope of 50 mV $dec^{-1}$, an onset potential of 120 mV, and an excellent electrochemical durability (Fig. 2.5.3c-e) [47]. The reason is that the rich defects result in exposing additional active edge sites by partial breaking of the catalytically less active basal planes (Fig. 2.5.3b). The conductivity of the defect-rich $MoS_2$ ultrathin nanosheets can be improved by the effective oxygen incorporation, and the oxygen-incorporated $MoS_2$ shows an improved onset overpotential, large cathodic current density and excellent cycling stability[48]. Furthermore, it is expected that 1T phase of $MoS_2$ with metallic nature of sulfide edge may enhance the catalytic activity. The metallic 1T $MoS_2$ nanosheet can be obtained by exfoliation with Li intercalation, as shown in Fig. 2.5.4a[49]. The obtained 1T $MoS_2$ exhibited more enhanced HER catalysis than 2H $MoS_2$, with the onset potential of 150 mV and a Tafel slope of 43 mV $dec^{-1}$ (Fig. 2.5.4b) [49]. Then, Voiry *et al.* prepared metallic 1T $MoS_2$ nanosheet by using an intercalation method without solvent. It exhibited dramatically enhanced catalytic activity for HER with a low Tafel slope of 40 mV $dec^{-1}$[50]. The result indicates that phase engineering is able to improve charge transfer kinetics in metallic $MoS_2$, playing a vital role in HER process. However, it is still a great challenge to investigate the catalytic property for the 1T phase in detail due to its poor stability.

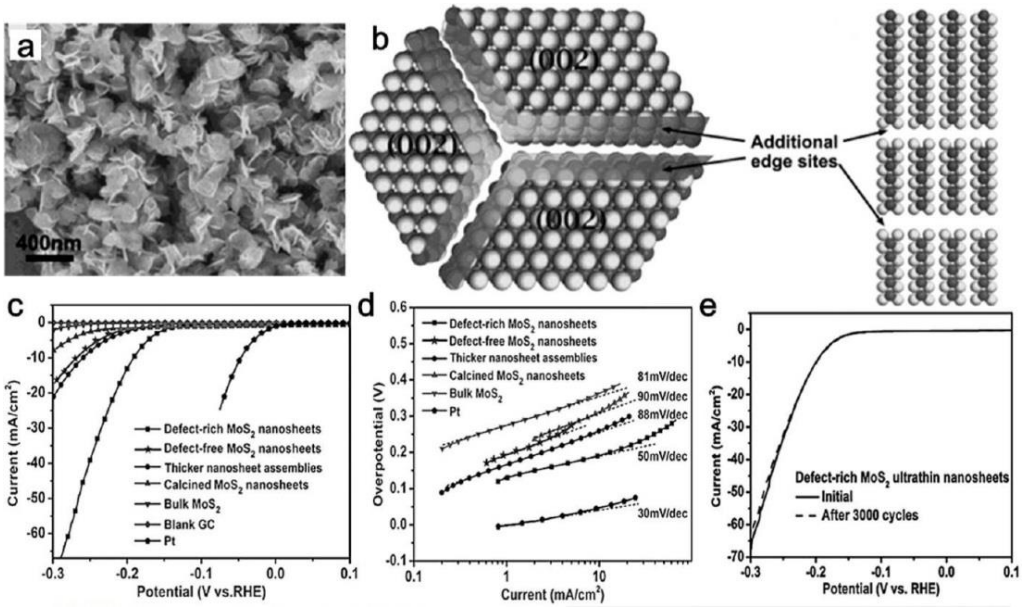


**Figure 2.5.3** (a) SEM image of $MoS_2$ nanosheet. (b) Atomic reconstruction of (a). (c) Polarization curves of various samples and (d) corresponding Tafel plots. (e) Durability test after 3000 CV cycles[47].

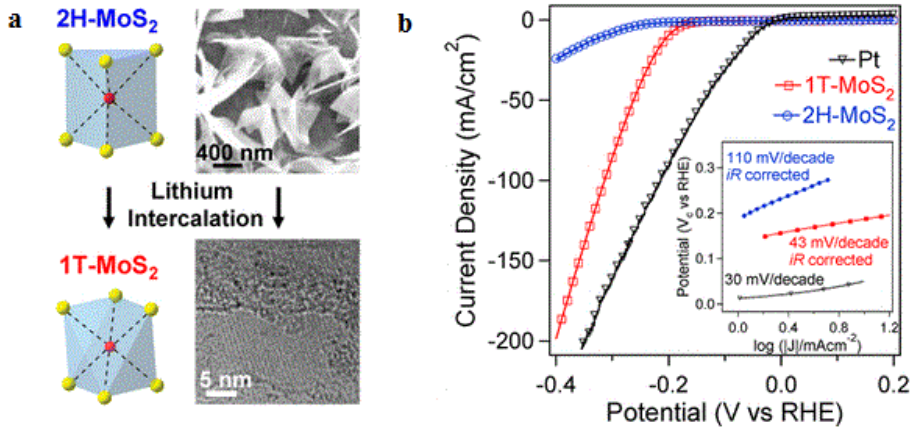


**Figure 2.5.4** (a) $MoS_2$ images characterized by SEM and TEM. (b) Corresponding polarization curves[43].

### 2.5.2 Energy storage

Li-ion battery (LIB), the most promising energy storage system, has high potential and low atomic weight, resulting in large energy density with a theoretical value of 400 Wh/kg[51]. The layered material like metal dichacolgenide has the interlayer spacing. They can hold different species, such

as $Li^+$ ion. Bulk $MoS_2$ is able to be used as the LIB electrode due to lithium ion insertion or extraction. But the structure of $MoS_2$ is not stable during the exfoliation process. Moreover, it suffers from the low energy density, leading to its limit as cathode materials. It is noteworthy that $MoS_2$ nanosheet can be considered as anodes for LIB owing to the structure stability[52]. There are many parameters to affect the performance of $MoS_2$ nanosheet as an effective anode material in LIB, such as conductivity, morphology, structure, size, and so on.

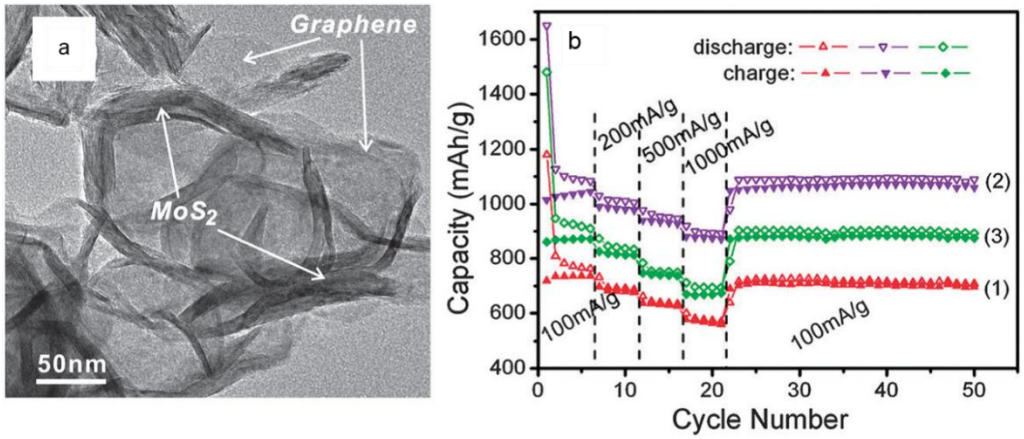


**Figure 2.5.5** (a) TEM image of $MoS_2$/graphene material. (b) Rate capability of $MoS_2$/graphene samples at different current density[53].

For the bulk $MoS_2$, the charge capacity is significantly degraded from 800 mA h $g^{-1}$ to 226 mA h $g^{-1}$ after 50 cycles. In contrast to bulk $MoS_2$, the restacked $MoS_2$ maintained the capacity above 750 mA h $g^{-1}$ after 50 cycles, displaying high charge storage capacities. This may be due to the increasing layer spacing[54]. The performance of $MoS_2$ anode could be further improved in the presence of poly(ethylene oxide). It was found that poly(ethylene oxide) can stabilize the disordered structure during the repeated cycles. Moreover, with the increase of amount of PEO, the spacing between layers of $MoS_2$ nanosheets was increased, which is advantageous for improving the capacity of $MoS_2$ nanosheet[55]. It is interesting to note that $MoS_2$/graphene, prepared by L-cysteine assisted hydrothermal process, can further improve the specific

capacities as well as the cycling performance because of the robust mechanical characteristics from the composite materials and synergistic effects between graphene and $MoS_2$[53]. With an appropriate Mo:C molar ratio, the material showed highest specific capacity of 1100 mA h $g^{-1}$ at a current of 100 mA $g^{-2}$ and high-rate capability (Fig. 2.5.5). It is challenging to solve the capacitive loss in the first cycle for $MoS_2$-based anodes. All in all, it is a promising anode material in the future for energy storage applications.

### 2.5.3 Electronic devices

Graphene-based electronic devices have been attracted tremendous attention because of the unique electrical and optical properties. Compared to graphene, $MoS_2$ has an indirect (1.29 eV) and direct band gap (1.9 eV) in the bulk and monolayer, respectively[56]. It opens up a new way for the next generation electronic devices. Simulations and theoretical studies expected that single-layer $MoS_2$ is available for an active-layer in devices with high mobility up to 350 $cm^2$/Vs at room temperature, high on/off ratios over 10 orders as well as a transconductance of 4.4 ms/μm[57], implying that dielectric engineering by using high-κ dielectrics is an efficient route to achieve high mobility devices through screening of charge impurities. Das *et al*. explained a mode to interpret the current flow patterns related to the charge impurity scattering in $MoS_2$[58]. As shown in Fig. 2.5.6, a resistor network composed of monolayer and van der Waals gap between the layers is applied to describe the current flow in a multi-layer $MoS_2$. Interestingly, the current mainly flows in upper layers regardless the amount of various gate biases. In addition, “hot spot” can be found when the layers are close to the source and the drain contacts. The predictions have successfully explained high-performance devices by 2D materials including $MoS_2$ for next generation devices.

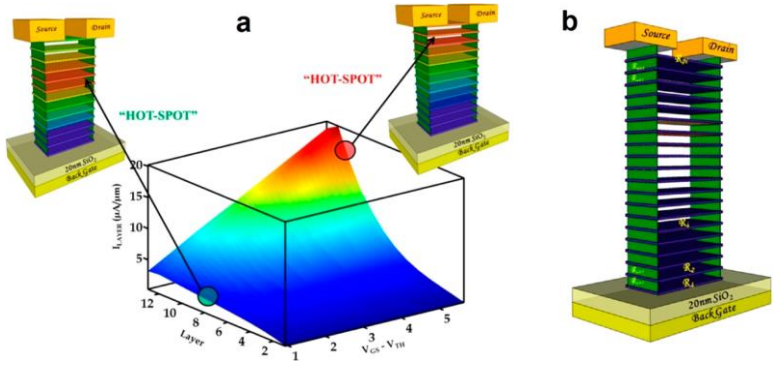


**Figure 2.5.6** Current distributions in a multilayer $MoS_2$. (a) Movement of current distributions in multilayer $MoS_2$ devices depending on various gate voltages. (b) A schematic of a resistor network model for multilayer $MoS_2$ systems[58].

The very first $MoS_2$ few layer field effect transistor (FET) exhibited low carrier mobilities in the range of 0.5-3 $cm^2\ V^{-1}\ s^{-1}$[24]. In order to enhance the mobility, Radisavljevic *et al.*[10] used $HfO_2$ high-κ gate dielectric as the tope gate dielectric, as shown in Fig. 2.5.7. The transistor exhibited the mobility of 200 $cm^2\ V^{-1}\ s^{-1}$ and room-temperature current on/off ratio exceeding $10^8$, which open up a way in electronics application based on two dimensional materials. Recently, high mobility of 100 $cm^2\ V^{-1}\ s^{-1}$ for the bottom-gated $MoS_2$ FET device[59] and 170 $cm^2\ V^{-1}\ s^{-1}$ for the top-gated $MoS_2$ FET device[60] as well as 517 $cm^2\ V^{-1}\ s^{-1}$ for the dual-gated $MoS_2$ FET device[61] can be obtained using $Al_2O_3$ as the high-κ dielectric. In addition, ionic liquids have been used as a dielectric material to improve the mobility of $MoS_2$ device[62].

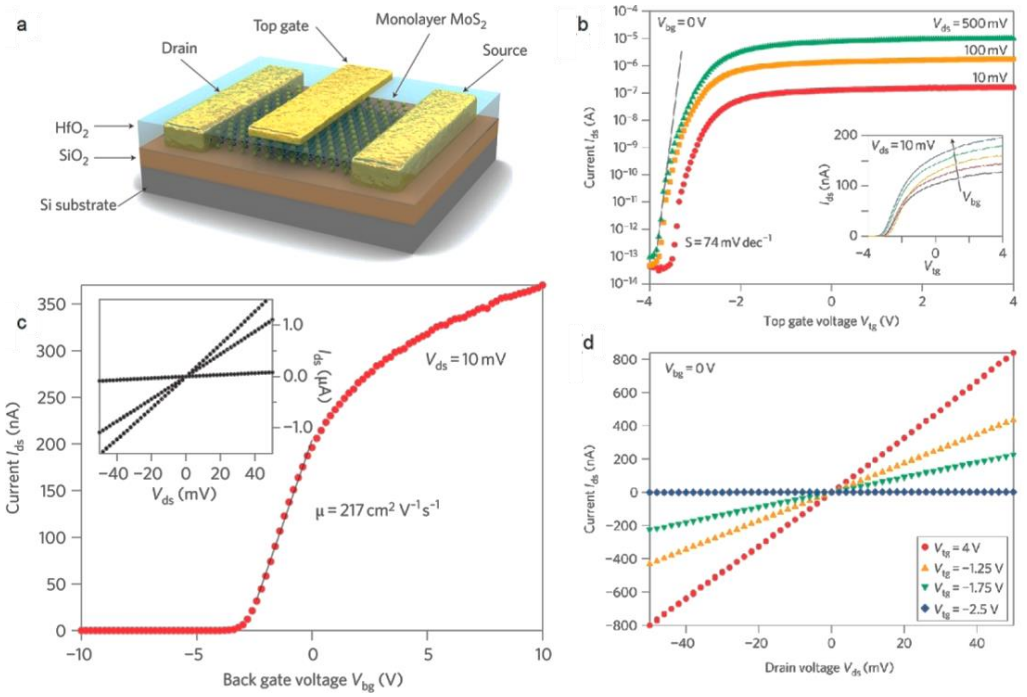


**Figure 2.5.7** (a) Schematic of a top-gate monolayer $MoS_2$ field effect transistor with a high-κ $HfO_2$ gate dielelctric. Transfer characteristics of a top-gated (b) and back gated (c) monolayer $MoS_2$ field effect transistor. (d) Output characteristic of monolayer $MoS_2$ field effect transistor[54].

The direct transition optical gap in $MoS_2$ makes it a promising candidate for optoelectronic application. Earlier $MoS_2$ optoelectronic device exhibited rapid switching times of 50 ms and a considerable photocurrent when the light was irradiated with the wavelength less than 670 nm[63]. The performance of $MoS_2$ phototransistor has been improved by using high-κ $Al_2O_3$ as gate dielectric. The device had a short carrier lifetime of 1.27 ns and a larger photoresponsivity of >100 mA/W[64]. Tsai *et al.*[65] developed metal-semiconductor-metal photodetectors by using few-layered $MoS_2$, which can be used in harsh environments. This device showed a high broadband gain up to 13.3, a rapid response time of 70 μs and short carrier lifetime of 110 μs, as shown in Fig. 2.5.8. It is worth mentioning that the photoresponsisvity up to 880A/W has been obtained for monolayer $MoS_2$ devices[66], which is attributed to the direct

bandgap of monolayer $MoS_2$. The monolayer $MoS_2$ has been suggested as a promising candidate for application in optoelectronics.

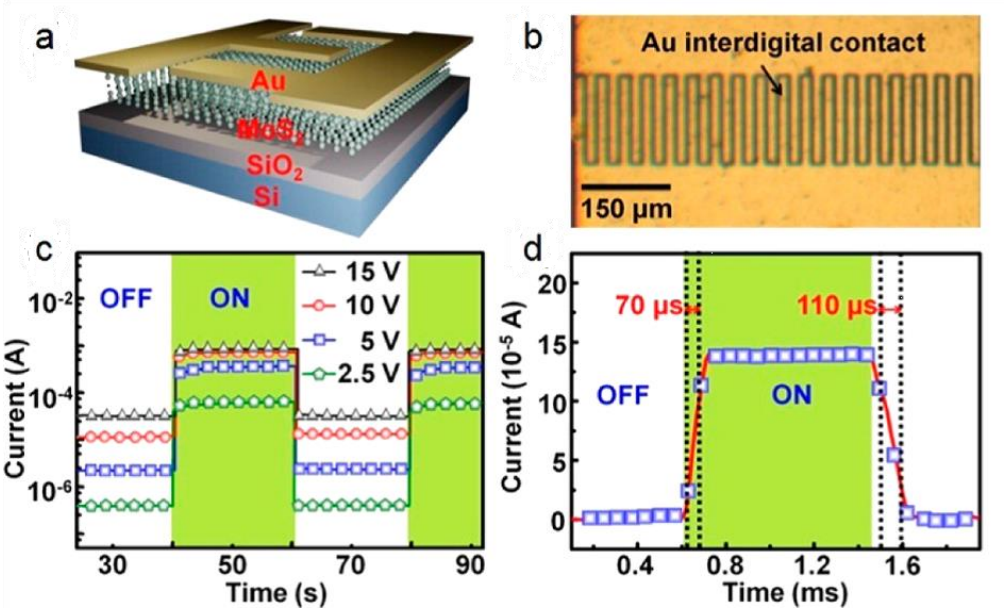


**Figure 2.5.8** (a) Schematic and (b) optical image of $MoS_2$ photodetector. Photoresponse (c) and high-resolution time response of $MoS_2$ photodetector in the dark and under laser illumination[68].

### 2.5.4 Sensors

In addition to the intriguing electronic and optoelectronic properties, $MoS_2$ has high surface-to-area ratios due to the two dimensional structure. Based on this merit, the $MoS_2$ has potential for the application in FET sensing, which can be used to detect organic molecular, biological molecular and gas. Up to now, gas molecules, such as NO, $NO_2$, $NH_3$ and so on, have been detected by monolayer or few layer $MoS_2$. For example, Dattatray *et al.*[67] developed few-layered $MoS_2$ FET sensor, which exhibited high sensitivity to $NO_2$ and $NH_3$, as showed in Fig. 2.5.9b. It was found that $NO_2$ caused an increase in the resistance while $NH_3$ caused a decrease in the resistance, which is based on a charge transfer mechanism. Upon exposure to triethylamine, the resistance of $MoS_2$-based FET sensor could decrease with increasing gas concentration, because triethylamine is a strong electron donor. This FET sensor showed high sensitivity toward

triethylamine[68]. In addition, $MoS_2$-based FET sensor can be used to detect pH changes of the electrolytic solution and biomolecules (streptavidin) [69]. In a wide pH range of 3 to 9, the device showed ultrahigh sensitivity (713 for a pH change of 1 unit). For streptavidin detection, the sensitivity is as high as 196, when the concentration of streptavidin is 100 femtomolar. Both pH and protein sensing can obtain high sensitivity in the subthreshold region. From the experimental results, $MoS_2$–based biosensors could be a promising candidate for next-generation diagnostics.

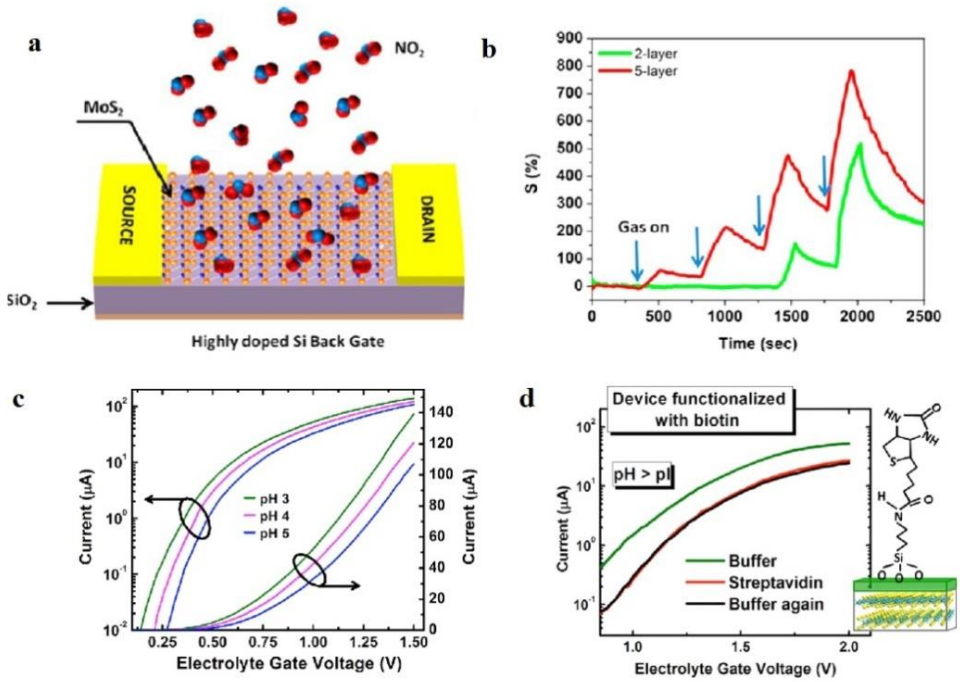


**Figure 2.5.9** (a) Illustration of $MoS_2$ transistor-based $NO_2$ gas sensing device. (b) Real-time current response to $NO_2$ exposure with increasing concentration[67]. (c) Drain current as a function of gate voltage for $MoS_2$ FET-based pH sensor. (d) $MoS_2$ FET sensor for detection of streptavidin[71].

## 2.6 Questions to be answered based on literature review

As discussed in the aforementioned literature review, tremendous progress has been achieved in the synthesis and preparation for layered TMDs, and various

applications have been researched. In spite of those effort, there are still several questions to be answered for further investigation.

First, several reports have been achieved to synthesize metallic-phase group-VI TMDs, but they was only able to obtain the mixture of metallic and semiconducting phases or the metallic phase with the small lateral size of less than micrometers. One may wonder whether it is possible to synthesize metallic-phase group-VI TMDs with lateral size up to hundreds of micrometers or not, and the product is large enough to investigate intrinsic properties of the metallic-phase group-VI TMDs? In addition, is it possible to distinguish electrocatalytic properties of different phases in $MoS_2$?

Second, it has been confirmed that $MoS_2$ can be exfoliated into few layer nanosheets by solution process, and the exfoliated $MoS_2$ nanosheets are considered as the electrical conductive material. By using electrical conductive materials, there have been immense research interest on artificial electronic skins. Especially, human skin provides human median nerve with distinct signals, enabling the brain to distinguish the touch and press. Is it possible to mimic those capability of human skin for developing $MoS_2$-based touch sensor?

## 2.7 PhD in context of literature

The focus on this thesis is preparation of metallic 1T'-$MoX_2$ (X=S, Se) crystals, and exploration of its electrochemical properties depending on different phases. The aforementioned questions are addressed in the following contents. The contribution of my thesis is in this part is listed as follows:

First, a facile method has been developed for preparation of 1T'-$MoX_2$ (X=S, Se) crystals. The obtained crystals have the lateral size of hundreds of micrometers. The atomic arrangement in different phases of $MoS_2$ is carefully characterized

by the aberration-corrected scanning transmission electron microscopy and selected area electron diffraction (SAED) patterns. Additionally, due to its metastable nature, the phase transformation from 1T'-$MoS_2$ to 2H-$MoS_2$ is achieved by thermal annealing and laser irradiation. Based on the 1T'-$MoS_2$ crystal and phase transformation, the electrocatalytic properties are demonstrated for the basal plane in $MoS_2$ with different phases.

Second, a skin-inspired sensor that is possible to distinguish touch and pressure has been demonstrated by mimicking rapidly adapting receptors and slowly adapting receptors by using $MoS_2$ nanosheet solution. The thin-film prepared by nanosheet solution are electrically conductive and the resistivity and transparency could be controlled by the amount of nanosheet solution. The skin-inspired $MoS_2$ sensor distinguished a touch of bare fingertip, and the touch and pressure could be discriminated by the different pattern from electrical signals.

**References:**

[1] K. S. Novoselov, *et al. Science* **2004**, 306, 666-669.

[2] A. H. Castro Neto, F. Guinea, N. M. R. Peres, K. S. Novoselov, and A. K. Geim. *Rev. Mod. Phys*. **2009**, 81, 109-162.

[3] A. S. Mayorov, *et al. Nano. Lett.* **2011**, 11, 2396-2399.

[4] J. S. Bunch, *et al. Nano Lett.* **2008**, 8, 2458-2462.

[5] M. Osada, and T. Sasaki. *Adv. Mater.* **2012**, 24, 210-228.

[6] A. Ayari, E. Cobas, O. Ogundadegbe, and M. S. Fuhrer. *J. Appl. Phys.* **2007**, 101, 014507.

[7] K. F. Mak, K. L. He, J. Shan, and T. F. Heinz. *Nat. Nanotechnol.* **2012**, 7, 494-498.

[8] M. Chhowalla, *et al. Nat. Chem.* **2013**, 5, 263-275.

[9] R. Bissessur, J.L. Schindler, C.R. Kannewurf, M. Kanatzidis, Mol. Cryst. Liq. Cryst. **1994**, 245, 249.

[10] B. Radisavljevic, A. Radenovic, J. Brivio, V. Giacometti, and A. Kis. *Nat. Nanotechno.* **2011**, 6, 147-150.

[11] C. Ataca, H. Sahin, and S. Ciraci. *J. Phys. Chem. C* **2012**, 116, 8983-8999.

[12] J. A. Wilson, and A. D. Yoffe. *Adv. Phys.* **1969**, 18, 193–335.

[13] S. Bertolazzi, J. Brivio, and A. Kis. *ACS Nano* **2011**, 5, 9703-9709.

[14] G. L. Frey, S. Elani, M. Homyonfer, Y. Feldman, and R. Tenne. *Phys. Rev. B* **1998**, 57, 6666-6671.

[15] A. Kuc, N. Zibouche, & T. Heine. *Phys. Rev. B* **2011**, 83, 245213.

[16] K. F. Mak, C. Lee, J. Hone, J. Shan, & T. F. Heinz. *Phys. Rev. Lett.* **2010**, 105, 136805.

[17] A. Splendiani, *et al. Nano. Lett.* **2010**, 10, 1271-1275.

[18] K. F. Mak, *et al. Nat. Mater.* **2013**, 12, 207-211.

[19] H. J. Conley, *et al. Nano Lett.* **2013**, 13, 3626-3630.

[20] C. Lee, *et al. ACS Nano* **2010**, 4, 2695-2700.

[21] A. Molina-Sanchez, and L. Wirtz. *Phys. Rev. B* **2011**, 84, 155413.

[22] B. Chakraborty, *et al. Phys. Rev. B* **2012**, 85, 161403.

[23] D. J. Late, *et al. ACS Nano* **2013**, 7, 4879–4891.

[24] K. S. Novoselov, *et al. Proc. Natl Acad. Sci. USA* **2005**, 102, 10451-10453.

[25] H. Li, *et al. ACS Nano* **2013**, 7, 10344-10353.

[26] J. N. Coleman, *et al. Science* **2011**, 331, 568-571.

[27] Y. G. Yao, *et al. J. Mater. Chem.* **2012**, 22, 13494-13499.

[28] R. J. Smith, *et al. Adv. Mater.* **2011**, 23, 3944-3948.

[29] A. O'Neill, U. Khan, and J. N. Coleman. *Chem. Mater.* **2012**, 24, 2414-2421.

[30] M. B. Dines. *Mater. Res. Bull.* **1975**, 10, 287-291.

[31] Z. Y. Zeng, *et al. Angew. Chem. Int. Ed.* **2011**, 50, 11093-11097.

[32] G. Eda, *et al. Nano Lett.* **2011**, 12, 526-526.

[33] Y. H. Lee, *et al. Adv. Mater.* **2012**, 24, 2320-2325.

[34] K. K. Liu, *et al. Nano Lett.* **2012**, 12, 1538-1544.

[35] Y. H. Lee, *et al. Nano Lett.* **2013**, 13, 1852–1857.

[36] Y. J. Zhan, Z. Liu, S. Najmaei, P. M. Ajayan, and J. Lou. *Small* **2012**, 8, 966-971.

[37] R. Hovden, *et al.* Proc. Nat. Acad. Sci. USA, **2016**, 113, 11420–11424.

[38] S. Cho, *et al. Science.* **2015**, 349, 625–628.

[39] P. Yu, W. Fu, Q. Zeng, J. Lin, C. Yan, Z. Lai, B. Tang, K. Suenaga, H. Zhang, Z. Li, *Adv. Mater.* **2017**, 29, 1701909.

[40] C. A. Papageorgopoulos, and W. Jaegermann. *Surf. Sci.* **1995**, **338**, 83–93.

[41] R. Bissessur, M. G. Kanatzidis, J. L. Schindler and C. R. Kannewurf. *J. Chem. Soc. Chem. Commun.*, **1993**, 20, 1582.

[42] M. Kan, *et al. J. Phys. Chem. C* **2014**, 118, 1515−1522.

[43] T. F. Jaramillo, *et al.* S*cience* **2007**, 317, 100-102.

[44] A. B. Laursen, S. Kegnæs, S. Dahl, and I. Chorkendorff. *Energy Environ. Sci.* **2012**, 5, 5577-5591.

[45] J. Kim, S. Byun, A. J. Smith, J. Yu, and J. Huang. *J. Phys. Chem. Lett.* **2013**, 4, 1227.

[46] Y. Yu, *et al. Nano Lett.* **2014**, 14, 553-558.

[47] J. Xie, *et al. Adv. Mater.* **2013**, 25, 5807-5813.

[48] J. Xie, *et al. J. Am. Chem. Soc.* **2013**, 135, 17881-17888.

[49] M. A. Lukowski, *et al. J. Am. Chem. Soc.* **2013**, 135, 10274-10277.

[50] D. Voiry, *et al. Nano Lett.* **2013**, 13, 6222-6227.

[51] M. R. Palacín. *Chem. Soc. Rev.* **2009**, 38, 2565-2575.

[52] Y. Teng, *et al. ACS Nano,* **2016**, 10, 8526–8535

[53] K. Chang, and W. Chen. *ACS Nano* **2011**, 5, 4720-4728.

[54] G. Du, *et al. Chem. Commun.* **2010**, 46, 1106–1108.

[55] J. Xiao, *et al. Chem. Mater.* **2010**, 22, 4522-4524.

[56] S. Balendhran, *et al. Nanoscale* **2012**, 4, 461-466.

[57] Y. Yoon, K. Ganapathi, S. Salahuddin. *Nano Lett.* **2011**, 11, 3768-3773.

[58] S. Das, and J. Appenzeller. *Nano Lett.* **2013**, 13, 3396-3402.

[59] S. Kim, *et al. Nat. Commun.* **2012**, 3, 1011.

[60] S. W. Min, *et al. Nanoscale* **2013**, 5, 548-551.

[61] H. Liu, & P. D. Ye. *IEEE Electron Device Lett.* **2012**, 33, 546– 548.

[62] Y. Zhang, J. Ye, Y. Matsuhashi, and Y. Iwasa, *Nano Lett.* **2012**, 12, 1136-1140.

[63] Z. Yin, *et al. ACS Nano* **2011**, 6, 74-80.

[64] W. Choi, *et al. Adv. Mater.* **2012**, 24, 5832-5836.

[65] D.-S. Tsai, *et al. ACS Nano* **2013**, 7, 3905-3911.

[66] O. Lopez-Sanchez, D. Lembke, M. Kayci, A. Radenovic, and A. Kis, *Nat. Nanotechnol.* **2013**, 8, 497-501.

[67] D. J. Late, *et al. ACS Nano* **2013**, 7, 4879-4891.

[68] F. K. Perkins, *et al. Nano Lett.* **2013***,* 13, 668-673.

[69] D. Sarkar, *et al. ACS Nano* **2014**, 8, 3992-4003.

# Chapter 3

# Experimental Methodology

*The rationale for selection of methods and materials is discussed, in this chapter. The chemicals and experimental procedures are described in detail. Subsequently, the methodology for characterization of results is explained, and then, device fabrication is illustrated.*

## 3.1 Rationale for materials and method selection

In the first part of the thesis, the layered TMDs, especially, $MoS_2$ and $MoSe_2$ were selected as the target materials and flux method was used to prepare phase-controlled crystals. From the materials of view, those TMDs are proper candidates because phase transition in those materials are relatively well explained as representatives among 2D materials. In group VI TMDs, the lithium intercalation is dominant process for phase transition. Based on the study on lithium intercalation, my goal has been utilization of the process into flux method. From the method point of view, flux method is attractive to prepare large size single crystals. From conventional methods such as n-butyl lithium solution or lithium intercalation by electrochemical process, it is the limit to prepare large size flakes due to the fractures by sonication or hydrogen evolution. The limit has hindered investigation on intrinsic properties of the materials. Therefore, it is of great importance for the phase-controlled synthesis to study on phase-dependent intrinsic property in TMDs.

## 3.2 Chemicals and synthesis process

### 3.2.1 Chemicals

Potassium molybdate ($K_2MoO_4$, 98%), Sulfur powder (S, 99.5%), Selenium powder (Se, 99.5%), Iodine ($I_2$, 99.8%) and Acetonitrile (99.8%) were purchased from Sigma Aldrich. Hydrogen (20% $H_2$ / 80% Ar) and purified Argon (Ar, 99.9%) were purchased from Leeden National Oxygen Ltd. in Singapore. The deionized water was purified using Milli-Q System (Millipore, Billerica, MA, USA). All the materials were used as received without any further purification.

### 3.2.2 Synthesis of 1T'-$MoS_2$ crystals

In a typical procedure, $K_2MoO_4$ (500 mg) and S powder (500 mg) were mixed and then ground for 15 min. The obtained mixture was annealed at 450 $^oC$ for 1.5 h under the gas flow of $H_2$ (10 sccm) and Ar (190 sccm). After cooling to room temperature, the product was taken out and mixed with S powder (500 mg), and then annealed at 450 °C for 1.5 h under the gas flow of $H_2$ (10 sccm) and Ar (190 sccm). Subsequently, the reaction zone was heated to 850 °C in heating rate of 10 °C/min under the gas flow of $H_2$ (40 sccm) and Ar (160 sccm) and then maintained for 10 h. After cooling down to the room temperature at rate of 10 °C/min, the obtained powder was washed with DI water until the pH value of suspension was 7-8. Then, the powder precursor was stored in DI water for 24 h. After soaking in an $I_2$ acetonitrile solution (4 mmol, 15 ml) for 3 h, the powder was washed with DI water for one time. Finally, the 1T'-$MoS_2$ crystals were obtained after drying at room temperature in vacuum oven.

### 3.2.3 Synthesis of 1T'-$MoSe_2$ crystals

The synthesis procedure for 1T'-$MoSe_2$ was similar to that of 1T'-$MoS_2$ except that the S powder was replaced by the Se powder.

### 3.2.4 Preparation of 2H-$MoS_2$ and 2H-$MoSe_2$ crystals

The 2H-$MoS_2$ and 2H-$MoSe_2$ crystals were obtained by annealing 1T'-$MoS_2$ and 1T'-$MoSe_2$ crystals, respectively, at 200 °C for 2 h in Ar.

## 3.3 Characterization

It is required to choose proper techniques to confirm the experimental results such as the composition, crystal phase, morphology and other physicochemical properties. Especially, the way to recognize atomic arrangement is necessary to distinguish different crystal phase in atomically thin 2D materials. Several techniques have been developed for this purpose such as transmission electron microscopy (TEM) and Raman spectroscopy. In this section, several characterization techniques are briefly described for 2D TMD materials.

### 3.3.1 Scanning electron microscopy

Scanning electron microscopy (SEM) is a conventional technique extensively used for morphological characterization in various research field such as material science, chemistry, biology and etc. The SEM provides higher magnification than optical microscopy over two orders by replacing the light source with electron beam. Because the resolution of images is mainly determined by the wavelength of radiation and the shorter wavelength offers the better resolution, SEM which utilizes shorter wavelength of electrons facilitates high-resolution image. During irradiation of electrons to samples, various signals are generated with interaction between electrons and the samples including secondary electrons (SEs), back-scattered electrons (BSEs) and X-rays.[1] Even though the transmission electron microscopy offers higher magnification, the SEM is convenient to prepare specimens and affordable to diverse samples.

In this thesis, the SEM images were obtained on a field-emission scanning electron microscope (JSM-7600F) coupled with energy dispersive X-ray spectroscopy (EDS).

### 3.3.2 Transmission electron microscopy

The transmission electron microscopy (TEM) is a potent analytical technique in material science, chemistry and even biology[2]. The image from TEM is formed by collection of electrons which is interacted with samples as the electron beam is transmitted via samples. Due to the prerequisite, "transmission", the samples need to be satisfied with several requirements to obtain high-resolution images. First, the samples are thin enough to be transmitted by the electron beam. Second, the samples have to be stable in high vacuum condition. Third, the samples should be stable under the electron beam irradiation. Up to now, the TEM is one of the most powerful tools to investigate nanomaterials for crystallinity, lattice, grain boundaries, interlayer distance and elemental compositions. Especially, in 2D materials research area, TEM is indispensable because the physicochemical properties are highly related to its crystal structure, atomic arrangements and chemical compositions. Even, atomic-level defects such as atomic substitution, doping and vacancy are able to influence to their properties tremendously[3] due to atomically thin thickness of 2D materials. Therefore, it is inevitable to associate imaging techniques with atomic resolution for 2D material research. Additionally, because TEM enables selected area electron diffraction (SAED) and energy dispersive spectroscopy (EDS) to investigate crystal structure and chemical composition, it may have effectively led unprecedented pace to develop the research for 2D materials.

### 3.3.3 Raman spectroscopy

Raman spectroscopy is one of the spectroscopic technique used to characterize vibrational or rotational modes in molecules and materials[4]. It collects information from Raman scattering by irradiation of laser as a light source to samples. When the light is irradiated to samples, most of them interact with the samples by an elastic process (Rayleigh scattering) but a small amount of light is generated with inelastic scattering. In Raman study, we can obtain the

specific information of materials from the inelastic scattering. For 2D materials, Raman spectroscopy offers fast and non-destructive analysis with high spatial resolution which are ideal for fundamental characterization. Specifically, this method can effectively distinguish each 2D materials because they have different lattice vibrations with various chemical compositions. For example, $MoS_2$ and $MoSe_2$ are a tetragonal prismatic structure. Even though they are same crystal phase, $MoS_2$ and $MoSe_2$ have 2 and 1 Raman peaks, respectively because of the difference of chalcogen atom. Moreover, the Raman peaks are dependent on the layer numbers of several 2D materials because of the long-range coulomb interaction[5]. Therefore, it is possible to determine the material and layer numbers, simultaneously.

### 3.3.4 X-ray photoelectron spectroscopy

X-ray photoelectron spectroscopy (XPS) has been a widely used technique to study properties of atoms, molecules and surfaces such as chemical composition, chemical states and electronic states. The photoelectron from samples are generated by the photoemission process when high energetic electrons interact with samples. The photoemission follows an equation below:

$$hv = E_B + E_K$$

where hv is the initiating photon energy, $E_B$ is the electron binding energy relative to the vacuum level and $E_K$ is the kinetic energy of photoelectron. In addition, the reference of instrument needs to be considered, so that $E_B$ is replaced by $E_B + \phi_{ref.}$. From the binding energy, it is possible to identify the elemental composition at the any solid surface of materials. By XPS, the energy distributions of photoemission from samples can be plotted, spatial distributions of any specific element can be mapped, and the depth profile can be analyzed from 10 nm to several μm. Those functions in XPS involve unveiling the chemical states of elements to determine the crystal phase in TMDs. For example, the Mo 3d and S 2p core levels are shifted to higher binding energy up

to 1.1 eV when the Li coverage increases in $MoS_2$[6]. The core level shift in Mo and S is distinct feature to confirm each phase, including that the intercalation is accompanied with electron transfer between $MoS_2$ and Li to fill in the d orbital of Mo. In this thesis, the elemental compositions and phases of materials were determined by XPS.

**References:**


1. W. Yi, P.Vania. Scanning electron microscopy. In: Graciela W. P., Qin W. (eds) Nanotechnology research methods for foods and bioproducts. (2012)
2. M.L.G. Gil, A. Fernández Larios. Transmission electron microscopy. In: Reina M., De Andrés J., Hadzic A., Prats-Galino A., Sala-Blanch X., van Zundert A. (eds) Atlas of functional anatomy for regional anesthesia and pain medicine (2015).
3. Z. Lin, B. R. Carvalho, E. Kahn, R. Lv, R. Rao, H. Terrones, M. A. Pimenta, M. Terrones. *2D Mater.* **2016**, 3, 022002.
4. G. Gouadec, P. Colomban. *Prog. Cryst. Growth Charact. Mater.* **2007**, 53, 1-56.
5. A. Molina-Sa´nchez and L. Wirtz. *Phys. Rev. B: Condens. Matter Mater. Phys.*, **2011**, **84**, 155413.
6. C. A. Papageorgopoulos, W. Jaegermann. *Surf. Sci.* **1995**, 338, 83–93.

# Chapter 4*

## 1T' Phase $MoS_2$ and $MoSe_2$ Crystals

*Tremendous effort has been devoted to the phase-controlled synthesis of inorganic crystals, particularly the metallic-phase group-VI transition metal dichalcogenides (TMDs), in which the transition metals are Mo and W, and the chalcogens are S, Se and Te, because of their superior performance in electrocatalysis and energy storage compared with their semiconducting counterparts. Although several synthetic methods have been developed to prepare the metallic-phase $MX_2$ (M=Mo, W; X=S, Se), the obtained products always coexist with the thermodynamically stable semiconducting phase, severely retarding the exploration of their properties and applications. Here, we report the preparation of metallic-phase 1T'-$MoX_2$ (X=S, Se) bulk crystals in large scale. The distorted octahedral coordination structure and intrinsic electrical property of 1T'-$MoS_2$ crystals have been studied. Impressively, the 1T'-$MoS_2$ can be converted to 2H-$MoS_2$ after thermal annealing and laser irradiation. More importantly, the results of hydrogen evolution reaction (HER) carried out in electrochemical microcells prove the crystal phase-dependent electrocatalysis of $MoS_2$, i.e. the basal plane of 1T'-$MoS_2$ is much more active than that of 2H-$MoS_2$.*

* The content in this chapter has been published in Nature Chemistry (*Nat. Chem.* 2018, 10, 638-643)

## 4.1 Introduction

Crystal phase-controlled synthesis of inorganic materials is critically important since the crystal structure can significantly affect their physicochemical properties, such as magnetic[1], electrical[2], optical[3] and catalytic properties[4,5]. The group-VI transition metal dichalcogenides (TMDs), such as $MoS_2$ and $MoSe_2$, can exist in several polymorphs including 2H and 1T phases, depending on the coordination modes between the transition metal and chalcogen atoms[6]. The octahedral coordinated TMDs, i.e. 1T phase, exhibit metallic properties, whereas the trigonal prismatic coordinated TMDs, i.e. 2H phase, are typically semiconductors with band gap of 1–2 eV[7]. Importantly, the 1T phase TMDs, compared to the 2H phase TMDs, show superior performance in the catalytic hydrogen evolution and energy storage, since the charge transfer resistance is dramatically reduced in the metallic phase[8-10].

Until now, several strategies have been used to synthesize metallic-phase group-VI TMDs, such as the flux method[11], alkali metal intercalation[12-14], e-beam irradiation[15], plasma hot electrons transfer[16], mechanical strain[17], colloidal synthesis[18] and hydrothermal reaction[19]. However, the 1T phase of $MX_2$ (M=Mo, W; X=S, Se) is metastable and easily converted to the stable 2H phase[10]. Except the thermodynamically stable 1T'-$MoTe_2$ and 1T'-$WTe_2$[11], the aforementioned methods can only produce the mixture of metallic and semiconducting phase TMD nanomaterials with lateral size less than 10 μm[10,14,19], which severely retards the exploration on the electrical properties of metallic-phase $MX_2$ and their applications. Therefore, it is of critical importance to develop a method for producing metallic-phase $MX_2$ (M=Mo, W; X=S, Se) bulk crystals and then revealing their crystal phase-based properties and applications.

Here, we report a facile method for the crystal phase-controlled synthesis of 1T'-$MoX_2$ (X=S, Se) crystals with lateral size up to hundreds of micrometers, which have been characterized by the aberration-corrected scanning

transmission electron microscopy (STEM), X-ray photoelectron spectroscopy (XPS), X-ray absorption fine structure (XAFS) and Raman spectroscopy. The phase transformation from 1T'-$MoS_2$ to 2H-$MoS_2$ has been achieved using both thermal annealing and laser irradiation. Furthermore, as a proof-of-concept application, three kinds of electrochemical microcells with 1T'-$MoS_2$ or 2H-$MoS_2$ as working electrode have been fabricated. Our results demonstrate that the basal plane of 1T'-$MoS_2$ is highly efficient for HER with an onset overpotential of only 65 mV and a current density (j) of 607 mA $cm^{-2}$ at an overpotential (η) of 400 mV (vs. RHE) as compared to that of 2H-$MoS_2$.

## 4.2 Results and discussion

### 4.2.1 Crystal structure of 1T'-$MoS_2$

The crystal structures of 2H- and 1T'-$MoS_2$ are illustrated in Fig. 4.1, showing the symmetry difference between the trigonal prismatic coordinated 2H-$MoS_2$ and the distorted octahedral coordinated 1T'-$MoS_2$[6,20].

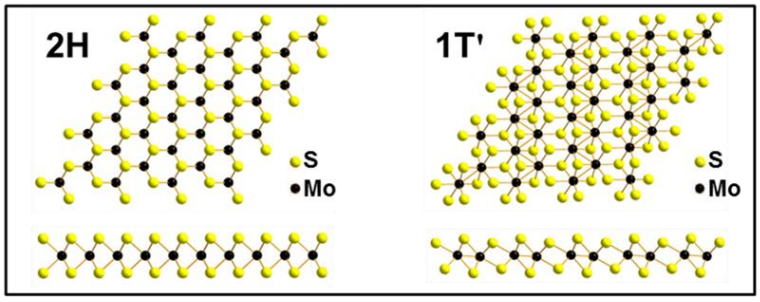


**Figure 4. 1** Schematic illustration of 2H- and 1T'-$MoS_2$ structures.

The synthetic method of 1T'-$MoS_2$ crystals is shown in detail in the Chapter 3. The scanning electron microscopy (SEM) image shows that the layered 1T'-$MoS_2$ crystals with lateral size up to hundreds of micrometers have been obtained (Fig. 4.2a). The energy-dispersive X-ray spectroscopy (EDS) gives strong signals of Mo and S elements with atomic ratio of ~1:2 (Fig. 4.2b), which is in consistent with the composition of $MoS_2$.

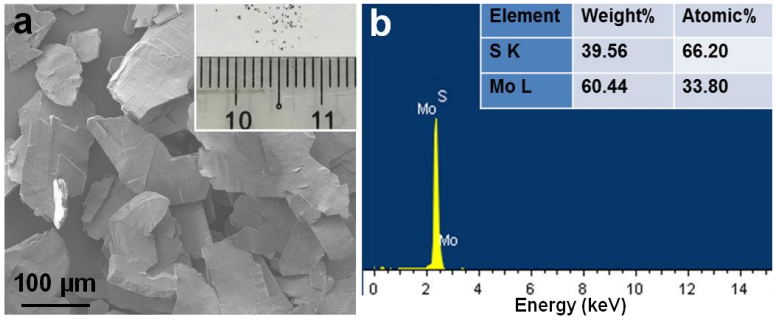


**Figure 4. 2** (**a**) SEM image and (**b**) EDS spectrum of the prepared 1T'-$MoS_2$ crystals. Inset in (**a**): A digital photograph of the obtained 1T'-$MoS_2$ crystals. Inset in (**b**): Atomic ratio of Mo and S obtained from the EDS spectrum.

The atomic structure of single-layer 1T'-$MoS_2$, obtained by mechanical exfoliation of 1T'-$MoS_2$ crystal, is revealed by STEM (Fig. 4.3a). The alternating one-dimensional bright and dark stripes are clearly observed, arising from the asymmetric distribution of Mo and S atoms, which is consistent with the structure of 1T'-$MoS_2$ as shown in Fig. 1a. Moreover, the corresponding fast Fourier transform (FFT) image (inset of Fig. 4.3a) proves the as-prepared layered 1T'-$MoS_2$ crystals with distorted octahedral coordinated structure. The selected area electron diffraction (SAED) patterns (Fig. 4.3c) obtained at different positions of one 1T'-$MoS_2$ crystal prove its distorted octahedral coordinated structure.

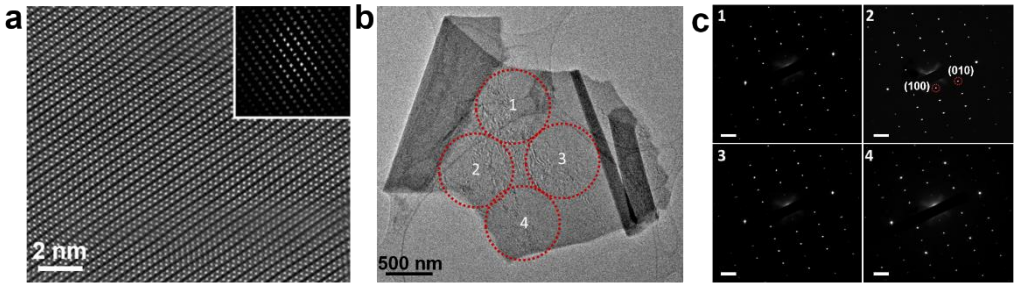


**Figure. 4. 3** (**a**) STEM image of single-layer 1T'-$MoS_2$ nanosheet. Inset: The corresponding FFT diffraction. (**b**) TEM image of a typical 1T'-$MoS_2$ crystal. (**c**) SAED patterns obtained from the corresponding positions in (**b**). The scale bars in (**c**) are 2 1/nm.

Based on the X-ray diffraction (XRD) characterizations (Figs. 1d,e), the peaks of 1T'-$MoS_2$ shift towards the higher degree as compared to the 2H-$MoS_2$ obtained by annealing 1T'-$MoS_2$ in Ar atmosphere at 200 °C for 2 h, consistent with their crystal structures[8]. Atomic force microscopy (AFM) characterization (Fig. 4. 5) reveals that the thickness of single-layer 1T'-$MoS_2$ nanosheet obtained by mechanical exfoliation is ~0.9 nm. All the aforementioned results confirm that 1T'-$MoS_2$ crystals have been successfully synthesized.

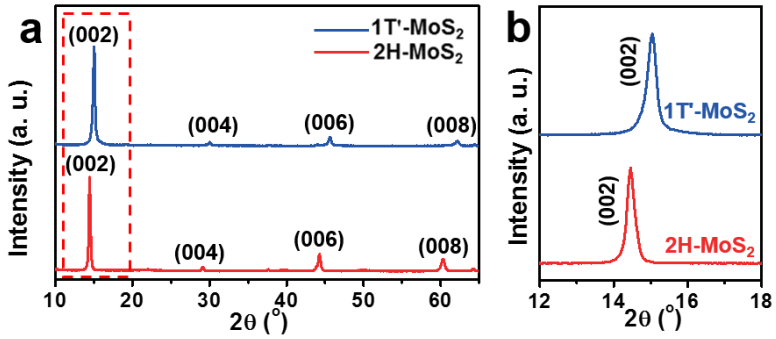


**Figure 4. 4** (**a**) XRD patterns of 1T'-$MoS_2$ crystals and 2H-$MoS_2$ crystals obtained by annealing 1T'-$MoS_2$ crystals. (**b**) Magnified XRD patterns of the (002) peaks of 1T'- and 2H-$MoS_2$ crystals, i.e. the red dashed area in (**a**).

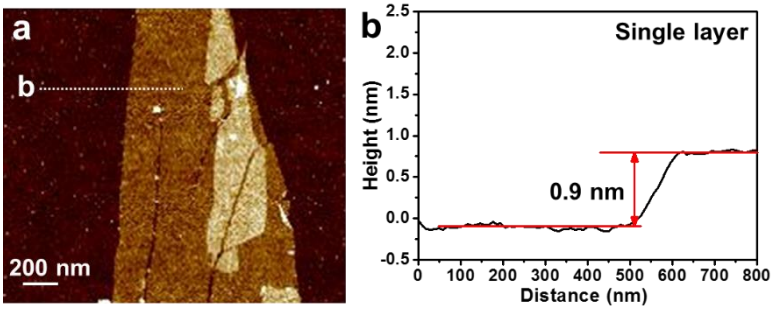


**Figure. 4. 5** (**a**) AFM image of mechanically exfoliated 1T'-$MoS_2$ nanosheet. **(b)** The thickness of single-layer 1T'-$MoS_2$ nanosheet measured from the corresponding white dotted line in (**a**).

### 4.2.2 Characterizations of 1T'- and 2H-$MoS_2$

To study the thermostability of 1T'-$MoS_2$ crystals, thermal gravimetric (TG) and differential scanning calorimetry (DSC) were performed in Ar atmosphere from 40 to 200 °C (Fig. 4.6a). An exothermic peak centered at 97.2 °C was observed.

However, the weight was preserved with the increase of temperature, indicating the phase transformation from the metastable 1T' phase to the thermodynamically stable 2H phase. Furthermore, TG-DSC was performed on the 2H-$MoS_2$ crystals (Fig. 4.6b), in which no exothermic peak appeared in this process, confirming that the thermal annealing can transform 1T'-$MoS_2$ to 2H-$MoS_2$, and the obtained 2H-$MoS_2$ crystals are thermodynamically stable. Moreover, the 1T'-$MoS_2$ and thermal-induced 2H-$MoS_2$ crystals are investigated by XPS (Fig. 4.7). The Mo 3d peaks of 1T'-$MoS_2$ located at 228.3 and 231.4 eV are corresponding to $3d_{5/2}$ and $3d_{3/2}$, respectively. Both of them showed shift of ~0.8 eV to lower binding energy as compared to the 2H-$MoS_2$[21].

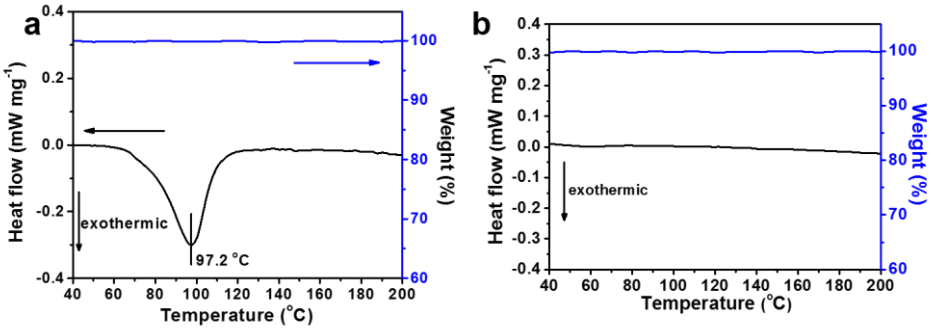


**Figure 4. 6** (a) TG-DSC curves of 1T'-$MoS_2$ crystals. (b) TG-DSC curves of 2H-$MoS_2$ crystals.

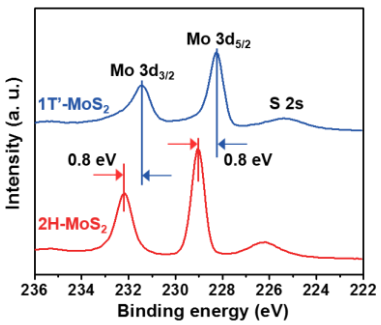


**Figure 4. 7** XPS Mo 3d spectra of 1T'-$MoS_2$ crystals and 2H-$MoS_2$ crystals obtained by annealing 1T'-$MoS_2$ crystals.

The XAFS spectra showed the lower chemical state in 1T'-$MoS_2$ crystals owing to the enrichment of electron on the surface (Fig. 4.8a) [15]. The variation tendency of interatomic distances for different shells obtained by theoretical calculation is consistent with the experimental XAFS results (Fig. 4.8b), confirming the thermal-induced phase transformation from the 1T'-$MoS_2$ crystals to 2H-$MoS_2$ crystals[22]. Furthermore, the thermal-induced phase transition process was confirmed by STEM (Fig. 4.9), in which the Mo zigzag chains in 1T'-$MoS_2$ were changed to the hexagonal arrangement in 2H-$MoS_2$. Simultaneously, S atoms arranged in asymmetry hexagonal structure around Mo atom in 1T'-$MoS_2$ were altered to the hexagonal arrangement with trigonal prismatic coordination with Mo in 2H-$MoS_2$.

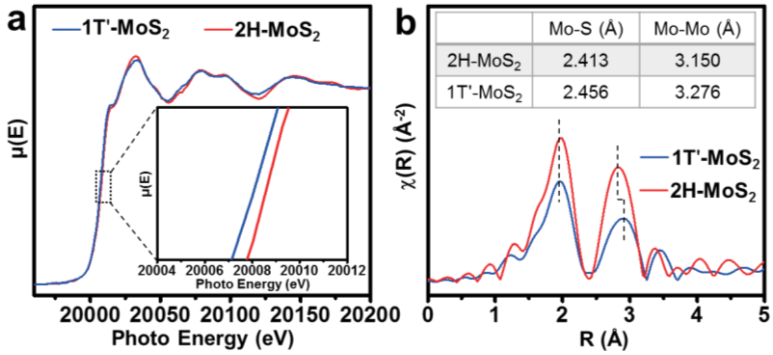


**Figure 4. 8** (**a**) Normalized XAFS spectra and (**b**) the corresponding Fourier transform of 1T'- and 2H-$MoS_2$ crystals. Inset in (**b**): Calculation results of the average Mo-S and Mo-Mo interatomic distances in 1T'- and 2H-$MoS_2$ crystals.

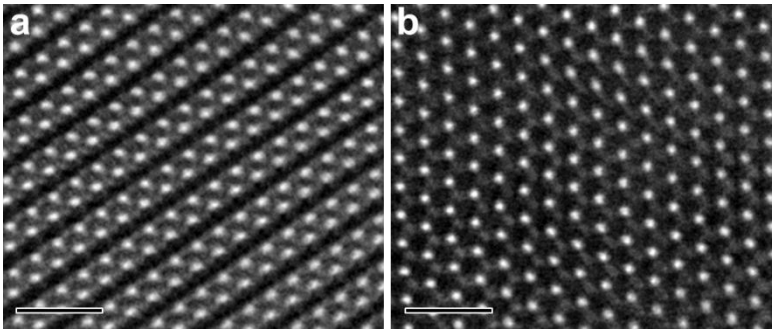


**Figure 4. 9** STEM images of the single-layer 1T'-$MoS_2$ nanosheet before (**a**) and after (**b**) thermal annealing. Scale bars: 1 nm.

The Raman spectra of 1T'- and 2H-$MoS_2$ flakes are presented in Fig. 4.10a. The 2H-$MoS_2$ flakes were prepared by annealing the 1T'-$MoS_2$ flakes obtained by mechanical exfoliation of 1T'-$MoS_2$ crystals. Two main Raman modes, i.e. $A_{1g}$ and $E_{2g}$, exist in as-obtained 2H-$MoS_2$ flakes. This result is consistent with the natural 2H-$MoS_2$ flakes[23]. As shown in Fig. 4.10a and Table 4.1, the distinct $J_1$, $J_2$, $J_3$ and $A_{1g}$ peaks appeared, while the characterization Raman peaks for 1T-$MoS_2$, i.e. $E_g$ (258 $cm^{-1}$) and $A_g$ (357 $cm^{-1}$), and the characteristic $E_{2g}$ peak (380 $cm^{-1}$) for 2H-$MoS_2$ were absent in the 1T'-$MoS_2$ due to the broken structural symmetry[24,25], revealing that our method has been successfully used to synthesize 1T'-$MoS_2$ crystals. The photoluminescence (PL) spectra of 2H- and 1T'-$MoS_2$ flakes are shown in Fig. 4.10b. Different from the metallic 1T'-$MoS_2$, two PL peaks, originated from the combination of interlayer coupling and spin-orbit coupling of 2H-$MoS_2$, are present, implying the bandgap opening of $MoS_2$ after the thermal annealing process[26].

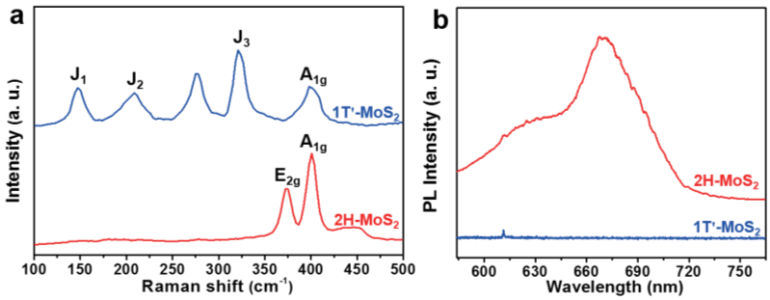


**Figure 4. 10** (**a**) Raman and (**b**) PL spectra of 1T'-$MoS_2$ flakes and 2H-$MoS_2$ flakes obtained by annealing 1T'-$MoS_2$ flakes.

**Table 4. 1** Comparison of Raman peaks for $MoS_2$ with different crystal phases.

| Experimental data ($cm^{-1}$) | Theoretical data ($cm^{-1}$) | | |
|---|---|---|---|
| As-prepared 1T'-$MoS_2$ flakes | 1T'-$MoS_2$ | 1T-$MoS_2$ | 2H-$MoS_2$ |
| 156 | 147; 151 | | |
| 218 | 216 | | |
| | 223 | | |
| | | 258 | |
| 287 | 286 | | |
| 333 | 333 | | |
| | 350 | | |
| | | 357 | |
| | | | 380 |
| 408 | 412 | | 402 |

Importantly, our method can also be used to synthesize the metallic 1T'-$MoSe_2$, which can also be converted to the stable 2H-$MoSe_2$ after thermal annealing, proving the generality of our method for preparation of metallic-phase bulk TMDs crystals (Figs. 4.11–14).

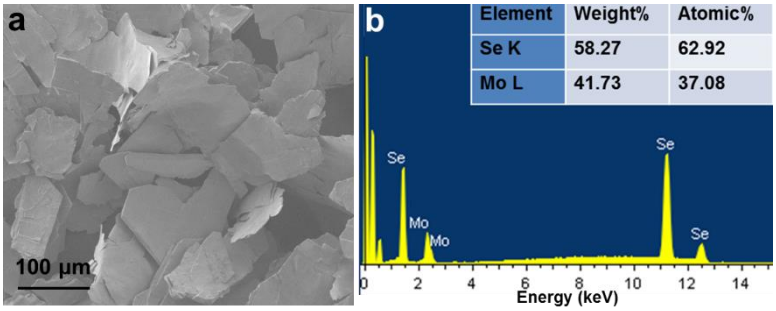


**Figure 4. 11** (**a**) SEM image and (**b**) EDS spectrum of the prepared 1T'-$MoSe_2$ crystals. Inset in (**b**): Atomic ratio of Mo and Se obtained from the EDS spectrum.

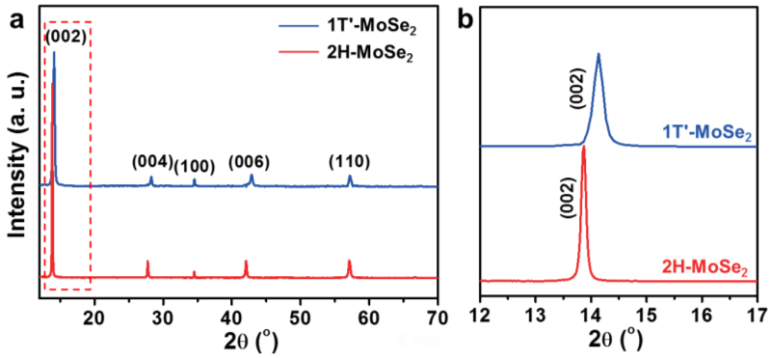

**Figure 4. 12** (**a**) XRD patterns of 1T'-$MoSe_2$ crystals and 2H-$MoSe_2$ crystals obtained by annealing 1T'-$MoSe_2$ crystals. (**b**) Magnified XRD patterns of the (002) peaks of 1T'- and 2H-$MoSe_2$ crystals, i.e. the red dashed area in (**a**).

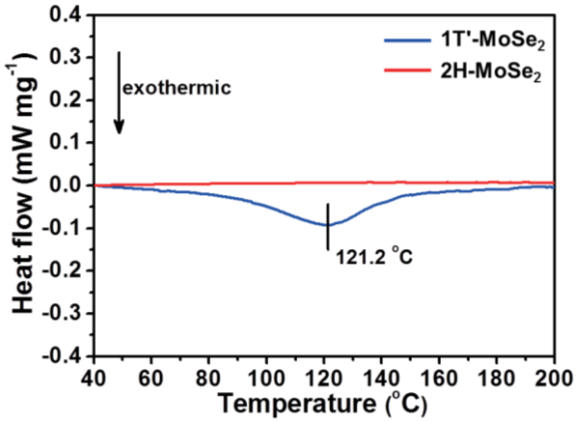


**Figure 4. 13** DSC curves of 1T'- and 2H-$MoSe_2$ crystals.

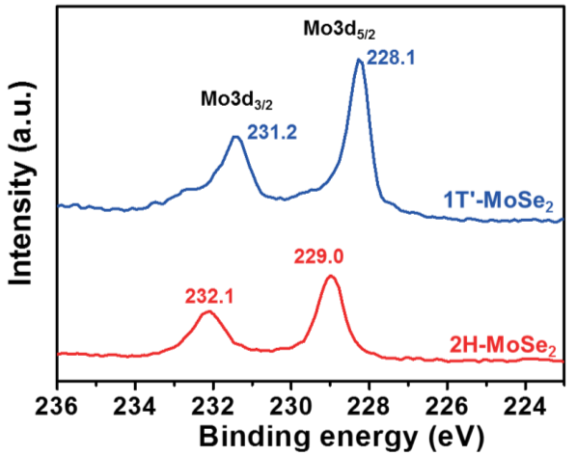


**Figure 4. 14** XPS Mo 3d spectra of the 1T'- and 2H-$MoSe_2$ crystals.

### 4.2.3 Laser-induced phase transformation from 1T'-$MoS_2$ to 2H-$MoS_2$

To achieve the controlled phase transformation from 1T'-$MoS_2$ to 2H-$MoS_2$, local phase patterning on a 1T'-$MoS_2$ flake was implemented by using laser irradiation. After two circular regions in a 1T'-$MoS_2$ flake were irradiated by laser, their color was obviously changed (Fig. 4. 15). Furthermore, the confocal Raman and PL were used to characterize the 1T'-$MoS_2$ flake before and after laser irradiation. The signals of $J_1$ mode of the 1T'-$MoS_2$ flake before and after

the laser irradiation at the circular regions are shown in Fig. 4. 16a and 4. 16b, respectively. It can be found that the signals of $J_1$ mode on the circular regions were extinct after laser irradiation. However, the signals of $E_{2g}$ mode of the 2H-$MoS_2$ were observed on the circular regions after the laser irradiation (Fig. 4. 16c). Furthermore, the PL signals of 2H-$MoS_2$ appeared on the circular regions after laser irradiation (Fig. 4. 16d). The corresponding Raman and PL spectra obtained from the laser-irradiated circular regions are displayed in Fig. 4. 16e and 4. 16f, respectively, showing the characteristic peaks of 2H-$MoS_2$. Importantly, the typical Raman peak of $MoO_3$ (~820 $cm^{-1}$) was not detected at the position of phase transformation (Fig. 4. 16e) [27]. All these results proved the phase transformation from 1T'-$MoS_2$ to 2H-$MoS_2$ in the selectively laser-irradiated regions.

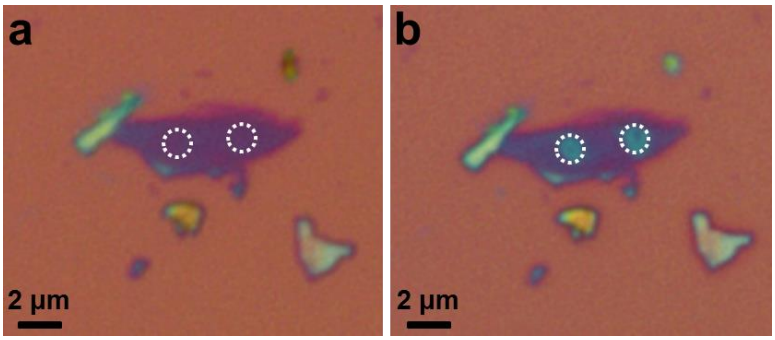


**Figure 4. 15** Optical images of a 1T'-$MoS_2$ flake before (**a**) and after (**b**) laser irradiation at two white dotted circular regions.

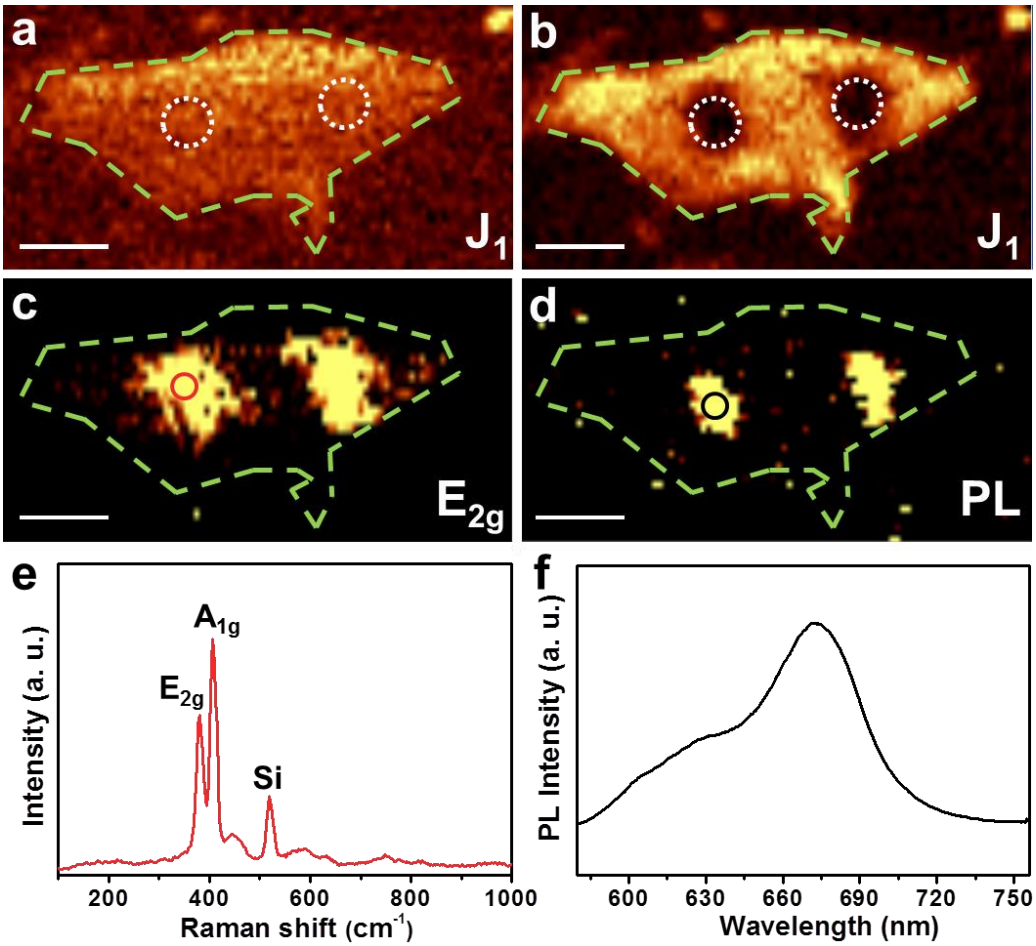


**Figure 4. 16** (**a, b**) Raman mapping images of a 1T'-$MoS_2$ flake obtained in the $J_1$ vibrational mode before (**a**) and after (**b**) laser irradiation at two white dotted circular regions. (**c**) Raman mapping image of the flake in (**b**) obtained in the $E_{2g}$ vibrational mode. (**d**) PL mapping image (580-755 nm) of the flake in (**b**). The green dashed lines in (a-d) represent the edge of $MoS_2$ flake. The scale bars in (**a-d**) are 2 μm. (**e**) Raman spectrum at the laser irradiated region, i.e. the red circle in (**c**). (**f**) PL spectrum at the laser irradiated region, i.e. the black circle in (**d**).

### 4.2.4 Phase-dependent HER measurements in electrochemical microcells

As a proof-of-concept application, after three kinds of electrochemical microcells, i.e. EM-1, EM-2, and EM-3, were fabricated (Fig. 4. 17a, see the Experimental Section), they were used for the electrocatalytic HER

measurements of the $MoS_2$ nanosheet exposed to the electrolyte (0.5 M $H_2SO_4$) (Figs. 4. 17b,c).

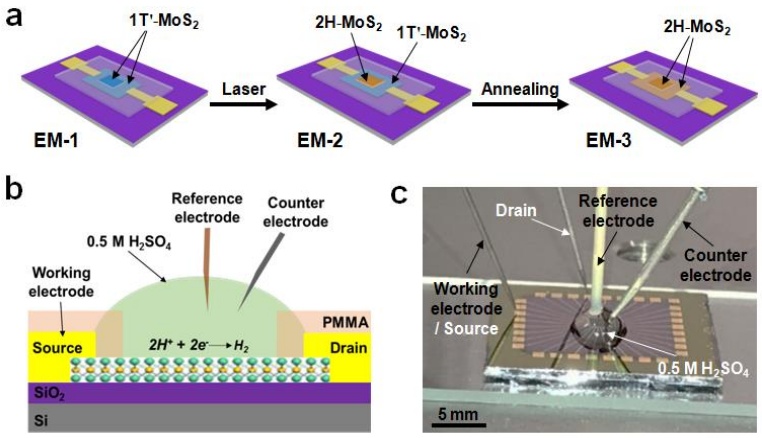


**Figure 4. 17** (**a**) Schematic illustration of fabrication of three kinds of electrochemical microcells (EM-1, EM-2 and EM-3). (**b**) Scheme of the electrochemical set-up for the electrocatalytic HER measurement on electrochemical microcells. (**c**) Photograph of the electrochemical set-up for the electrocatalytic HER measurement on electrochemical microcells.

Our measurements proved the contacts between the $MoS_2$ nanosheet and the Cr/Au electrodes are Ohmic contact for EM-1 and EM-2, and Schottky contact for EM-3 (Figs. 18-20).

The linearity of drain current ($I_d$) depending on the drain voltage ($V_d$) in 1T'-$MoS_2$ nanosheet-based device proves the Ohmic contact between the 1T'-$MoS_2$ nanosheet and the Cr/Au electrodes. The gate voltage ($V_g$) has no effect on the $I_d$, indicating the typical metallic properties of the 1T'-$MoS_2$ nanosheet with conductivity in range of 700-1000 S/m, which is calculated by Equations (1) and (2).

$$G = \frac{I}{V} = \sigma \frac{A}{l} \quad (1)$$

$$\sigma = \frac{I \times l}{V \times A} \quad (2)$$

where G (A/V) is conductance, V is voltage (V), I is current (A), $\sigma$ is electrical conductivity (S/m), A is cross-sectional area of the conductor ($m^2$) and $l$ is the length of conductor (m).

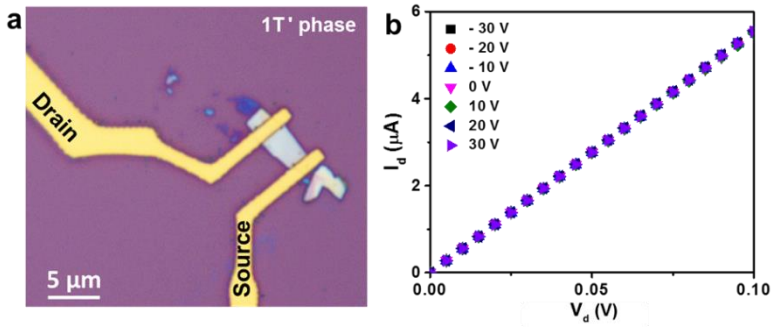


**Figure 4. 18** (**a**) Optical image of as-prepared 1T'-$MoS_2$ nanosheet-based device. (**b**) The conductance of 1T'-$MoS_2$ nanosheet-based device measured at gate voltage ($V_g$) ranging from -30 to 30 V.

In the 2H/1T'-$MoS_2$ nanosheet-based device, the 2H-$MoS_2$ channel was prepared in the 1T'-$MoS_2$ nanosheet. The two parts of 1T'-$MoS_2$ connected to the Cr/Au electrodes were linked by the 2H-$MoS_2$ channel (Fig. 4. 19a). The contacts between the 1T'-$MoS_2$ nanosheet and the Cr/Au electrodes, and between 2H-$MoS_2$ and 1T'-$MoS_2$ in the 2H/1T'-$MoS_2$ nanosheet are Ohmic contact based on the linearity of $I_d$ depending on $V_d$ (Fig. 4. 19b). It demonstrates that, during the HER measurement in EM-2, the electrons are transported from the Cr/Au electrode to the exposed area of 2H-$MoS_2$ via the Ohmic contact with the linkage of 1T'-$MoS_2$ between them, ensuring a highly efficient charge transport. In the 2H/1T'-$MoS_2$ nanosheet-based device, the conductance depending on $V_g$ was observed, further confirming the transformation of channel material from metallic 1T' phase to semiconducting 2H phase. It can be calculated that the on/off ratio of the 2H/1T'-$MoS_2$ nanosheet-based device prepared by laser-induced phase patterning is ~$10^3$ (Fig. 4. 19c). These results demonstrated that 2H channel with high quality can be obtained through laser-induced phase patterning.

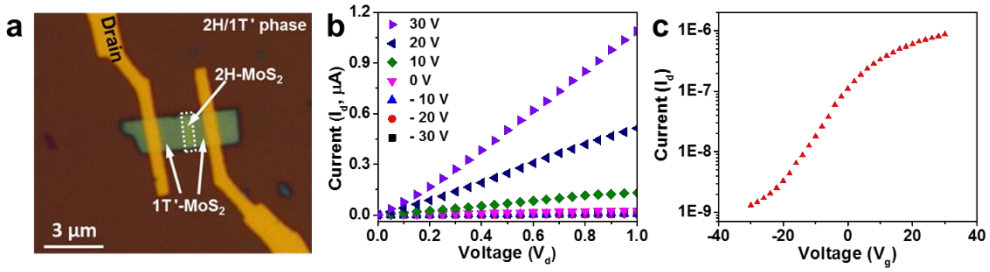


**Figure 4. 19** (**a**) Optical image of as-prepared 2H/1T'-$MoS_2$ nanosheet-based device. (**b**) The conductance of 2H/1T'-$MoS_2$ nanosheet-based device measured at $V_g$ ranging from -30 to 30 V. (**c**) Gate-voltage-dependent drain current ($I_d$-$V_g$) of 2H/1T'-$MoS_2$ nanosheet-based device at drain voltage ($V_d$)=1 V.

The nonlinearity relationship between $I_d$ and $V_d$ reveals the Schottky contact between the 2H-$MoS_2$ nanosheet and the Cr/Au electrodes. Its conductance is dependent on the $V_g$, confirming the n-type semiconducting properties in the 2H-$MoS_2$ nanosheet (Fig 4. 20).

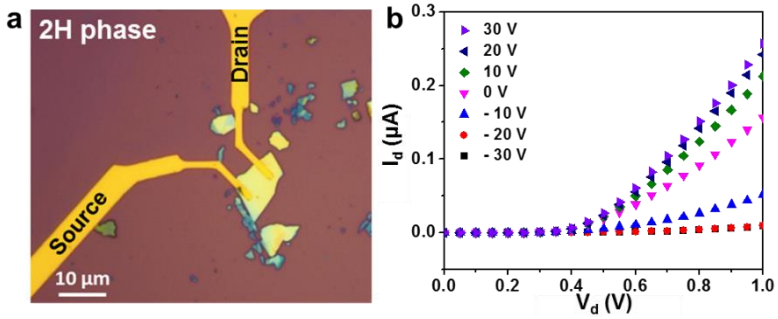


**Figure 4. 20** (**a**) Optical image of as-prepared 2H-$MoS_2$ nanosheet-based device. (**b**) The conductance of 2H-$MoS_2$ nanosheet-based device measured at $V_g$ ranging from -30 to 30 V.

As shown in Figs. 4. 21a and b, the basal plane of 1T'-$MoS_2$ in EM-1 shows remarkable HER performance with an onset overpotential of 65 mV and a current density of 607 mA $cm^{-2}$ at 400 mV (vs. RHE). However, in EM-2, after laser-induced phase transformation from 1T' to 2H in the exposed basal plane area of 1T'-$MoS_2$ nanosheet, the HER performance dramatically decreased with

onset potential of 200 mV and a current density of 43 mA $cm^{-2}$ at 400 mV (vs. RHE) (Figs. 4. 21a,b). After thermal annealing of EM-2, the phase of whole $MoS_2$ nanosheet changed from 1T' to 2H, resulting in the further decrease of the HER performance in EM-3 due to the Schottky barrier, i.e. high contact resistance, between the 2H-$MoS_2$ nanosheet and the Cr/Au electrodes (Fig. 4. 22) [28,29]. The aforementioned results demonstrate that the basal plane of 1T'-$MoS_2$ is much more active in the electrocatalytic HER compared to that of 2H-$MoS_2$, which could be attributed to the intrinsic distorted octahedral crystal structure in 1T'-$MoS_2$[20]. In addition, the metallic phase 1T'-$MoS_2$ shows better charge transport ability compared to the semiconducting 2H-$MoS_2$, contributing to the high HER performance, which is consistent with a previous report[30]. Although extensive research efforts have been devoted to investigation of the role of edges, doping, defects, and strain of TMDs and charge transport between TMDs and electrodes in electrocatalytic performances[30-32], our metallic phase 1T'-$MoS_2$ crystals provide a unique opportunity to study the effect on electrocatalysis solely based on the crystal phase. Our results proved the crystal phase-dependent electrocatalysis, offering a new insight into the design and synthesis of highly efficient catalysts.

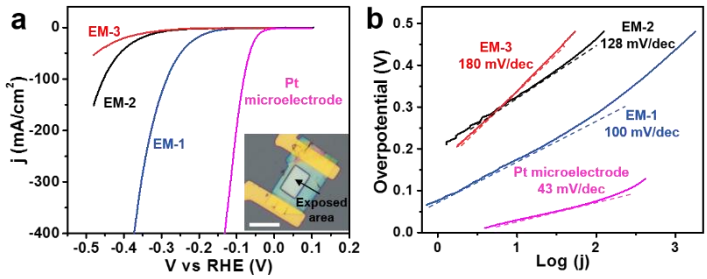


**Figure 4. 21** (**a**) Polarization curves obtained in EM-1, EM-2 and EM-3. Inset: Optical microscope image of EM-1. Scale bar: 20 μm. (**b**) Tafel plots obtained from the polarization curves in (**a**).

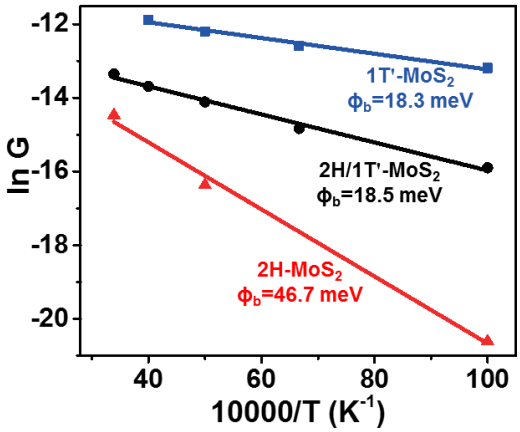


**Figure 4. 22** Arrhenius plots of the conductance for 1T'-, 2H/1T'- and 2H-$MoS_2$ nanosheet-based devices at $V_g$=40 V. The results confirm the high Schottky barrier between the 2H-$MoS_2$ nanosheet and the Cr/Au electrodes.

## 4.3 Conclusion

In summary, we report a facile and robust method to prepare the 1T'-$MoX_2$ (X=S, Se) crystals. The distorted octahedral coordination structure in 1T'-$MoS_2$ crystals is confirmed by the STEM, XPS, XAFS and Raman spectroscopy. The intrinsic optical and electrical properties of as-obtained 1T'-$MoS_2$ are characterized. The laser- and thermal-induced phase transformation from 1T'-$MoS_2$ to 2H-$MoS_2$ crystals has been achieved. Three kinds of electrochemical microcells used for the electrocatalytic HER measurements are constructed. The remarkable HER performance on the basal plane of 1T'-$MoS_2$ was found with an onset overpotential of 65 mV and a current density of 607 mA $cm^{-2}$ at 400 mV (vs. RHE), which is among the best in the $MoS_2$-based electrocatalysts. The excellent HER performance originates from the higher active basal plane and better charge transport ability of 1T'-$MoS_2$ compared to that of 2H-$MoS_2$. Our findings could open up a new avenue for preparation of metastable metallic-phase TMDs, and exploration of crystal phase-dependent properties and applications in electrochemical devices, catalysis, and so on.

**References:**


[1] S. Sun, C. B. Murray, D. Weller, L. Folks, A. Moser, *Science.* **2000**, 287, 1989–1992.

[2] C. Thelander, P. Caroff, S. Plissard, A. W. Dey, K. A. Dick, *Nano Lett.* **2011**, 11, 2424–2429.

[3] C. H. Park, B.-H. Cheong, K.-H. Lee, K. J. Chang, *Phys. Rev. B.* **1994**, 49, 4485–4493.

[4] J. Kim, Y. Lee, S. Sun, *J. Am. Chem. Soc.* **2010**, 132, 4996–4997.

[5] Z. Fan, *et al. J. Am. Chem. Soc.* **2016**, 138, 1414–1419.

[6] D. Voiry, A. Mohite, M. Chhowalla, *Chem. Soc. Rev.* **2015**, 44, 2702–2712.

[7] M. Chhowalla, *et al. Nat. Chem.* **2013**, 5, 263–275.

[8] M. A. Lukowski, *et al. J. Am. Chem. Soc.* **2013**, 135, 10274–10277.

[9] D. Voiry, *et al. Nat. Mater.* **2013**, 12, 850–855.

[10] M. Acerce, D. Voiry, M. Chhowalla, *Nat. Nanotechnol.* **2015**, 10, 313–318.

[11] D. H. Keum, *et al. Nat. Phys.* **2015**, 11, 482–486.

[12] M. A. Py, R. R. Haering, *Can. J. Phys.* **1983**, 61, 76–84.

[13] F. Wypych, R. Schollhorn, *J. Chem. Soc., Chem. Commun*. **1992**, 19, 1386–1388.

[14] Z. Zeng, *et al. Angew. Chem. Int. Ed.* **2011**, 50, 11093–11097.

[15] Y.-C. Lin, D. O. Dumcenco, Y.-S. Huang, K. Suenaga, *Nat. Nanotechnol.* **2014**, 9, 391–396.

[16] Y. M. Kang, *et al. Adv. Mater.* **2014**, 26, 6467–6471.

[17] K.-A. N. Duerloo, Y. Li, E. J. Reed, *Nat. Commun.* **2014**, 5, 4214.

[18] B. Mahler, V. Hoepfner, K. Liao, G. A. Ozin, *J. Am. Chem. Soc.* **2014**, 136, 14121–14127.

[19] X. Geng, *et al. Nat. Commun.* **2016**, 7, 10672.

[20] S. S. Chou, *et al. Nat. Commun.* **2015**, 6, 8311.

[21] Y. Yin, *et al. J. Am. Chem. Soc.* **2016**, 138, 7965–7972.

[22] D. Y. Chung, *et al. Nanoscale.* **2014**, 6, 2131–2136.

[23] H. Li, *et al. Adv. Funct. Mater.* **2012**, 22, 1385–1390.

[24] D. Yang, S. J.Sandoval, W. M. R. Divigalpitiya, J. C. Irwin, R. F. Frindt, *Phys. Rev. B.* **1991**, 43, 12053–12056.

[25] M. Calandra, *Phys. Rev. B.* **2013**, 88, 245428.

[26] A. Splendiani, *et al. Nano Lett.* **2010**, 10, 1271–1275.

[27] A. Castellanos-Gomez, *et al. Nano Lett.* **2012**, 12, 3187–3192.

[28] R. Kappera, *et al. Nat. Mater.* **2014**, 13, 1128–1134.

[29] S. Cho, *et al. Science.* **2015**, 349, 625–628.

[30] D. Voiry, *et al. Nat. Mater.* **2016**, 15**,** 1003–1009.

[31] T. F. Jaramillo, *et al. Science.* **2007**, 317, 100–102.

[32] H. Li, *et al. Nat. Mater.* **2016**, 15, 48–54 (2016).

# Chapter 5

## Skin-inspired $MoS_2$ tactile sensor

*Human skin plays a key role to communicate with circumstance by perception of the pressure, temperature, vibration, and etc. To mimic the human skin by electronics so-called e-skin, various electronic devices have been developed with functional nanomaterials, and some 2D materials are considered as one of the functional materials due to the electrical properties, chemical stability and high surface area to volume ratio. Particularly, $MoS_2$ thin film prepared by the Li intercalation method exhibited promising properties for the tactile sensors. In this chapter, I demonstrate a skin-inspired $MoS_2$ touch sensor with recognizing touch and press.*

## 5.1 Introduction

Human skin, a largest sensory organ covering our entire body, is multifunctional sensory system to recognize various external stimuli, allowing us to communicate and interact with circumstance. Due to the demand in wearable electronics, robotics and so on[1], the effort to make the artificial electronic skins (E-skin) has been boosted to mimic functions of the human skin which is possible to perceive the temperature and mechanical force including stretching, bending and touch. Capabilities such perceptions may enable them to extend their utilization such as diagnostic devices for real-time healthcare by monitoring hear rate and body temperature, and prosthetics[2,3].

Haptic perception of human skin is facilitated by four different mechanoreceptors which are 241 ea per square centimeter in fingertips and 58 in the palm and distributed in the various range of depth below the skin[4]. The four receptors are Pacinian corpuscle, Ruffini corpuscle, Merkel receptor and Meissner corpuscle classified by sensory function, stimuli and its locations. Pacinian corpuscle and Meissner corpuscle, called rapidly adapting receptors, detect temporal changes from skin deformation (e.g. vibration) while Ruffini corpuscle and Merkel receptor, called slowly adapting receptors, are possible to sense stationary force from stimuli. From the mechanoreceptors, human skin is allowed to detect the haptic perception with spatial resolution of 0.5 to 1 mm[5], vibrations up to 700 Hz[6], the pressure threshold up to 0.055 g and 0.019 g on the fingertips of men and women, respectively[7]. The performance of human skin could be the aim for E-skins.

In order to detect external stimuli in E-skins, the stimuli is required to be converted into electrical signals, and several strategies have been developed such as piezoresistivity[8,9], capacitance[10,11], piezoelectricity[12,13], transistor[14,15]. Especially, piezoresistive sensors have been tremendously studied due to proper accessibility originated from simple fabrication process

and high sensitivity. The sensors have commonly sandwiched structures consisting of flexible substrates and electrical conductive active layers. For the flexible substrates to provide devices with mechanical compliance, polydimethylsiloxane (PDMS) and its derivatives are largely used for supporting active materials in E-skins owing to intrinsic stretchability, easy figuration and commercial availability, and cellulose nanopaper[16] and silk[17] are also promising candidates. To find proper active materials for transducing external stimuli to electrical signals, electrically several conductive materials have been employed such as carbon nanotubes (CNT)[18,19], graphene[20,21], conductive nanowires[22,23]. Even though tremendous research effort has been made successful approach to the similar sensitivity with human skin[24,25], there are still remained obstacles to overcome for practical application with cost-effective, multifunctional and high sensitivity.

Transition metal dichalcogenides (TMDs) are a part of layered materials consisting of transition metal layers which is sandwiched by two chalcogen atoms. They are able to be exfoliated into single layer nanosheet structures by physical and chemical methods[26,27], allowing them to use as solution-processable materials. The nanosheets ink has great potential into electronics due to cost effectiveness and easy fabrication process[28], but they have not vigorously been studied in pressure sensor, yet.

Herein, I demonstrate a skin-inspired sensor that is possible to distinguish touch and pressure by mimicking rapidly adapting receptors and slowly adapting receptors by using $MoS_2$ nanosheet solution. The thin-film prepared by nanosheet solution are electrically conductive and the resistivity and transparency could be controlled by the amount of nanosheet solution. The skin-inspired $MoS_2$ sensor distinguished a touch of bare fingertip, and the touch and pressure could be discriminated by the different pattern from electrical signals.

## 5.2 Results and discussion

### 5.2.1 Characterization of the $MoS_2$ thin film

For the preparation of nanosheet solution, 50 mg of $MoS_2$ powders of were dispersed in 5 ml of 2 M N-butyl lithium in cyclohexane in glove box at room temperature. The vial with the mixed solution was stagnated for 2-3 days for the reaction. After the reaction, the supernatant was carefully decanted to a cleaned container and washed it by hexane for 2-3 times. The solution was further washed 2-3 times with deionized water by centrifugation (3000 rpm). The washed precipitation was dispersed into deionized water by sonication process. The aqueous $MoS_2$ solution was used for fabricating a $MoS_2$ film with the thickness of around 1-2 μm on AAO (anodic aluminum oxide) membrane with pore size of 200 nm by a vacuum filtration (Fig. 5.1a).

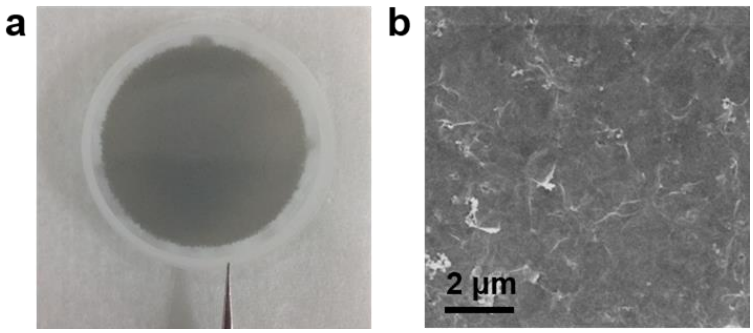


**Figure 5. 1** (a) An optical and (b) SEM image of $MoS_2$ film in AAO membrane by a vacuum filtration method.

The $MoS_2$ film is able to be transferred to other substrates. In this experiment, I transferred the thin film onto PDMS substrates for flexible devices.

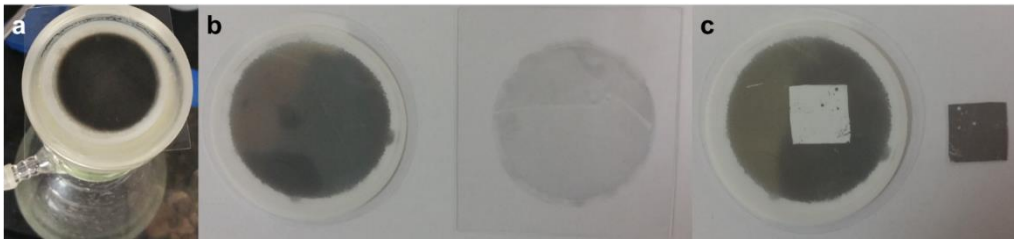


**Figure 5. 2** Optical images for a transfer process of $MoS_2$ thin film.

For the transfer, at first, the $MoS_2$ film is required to be fully dried to prevent from the surface interaction between $MoS_2$ film and PDMS by water. On the dried $MoS_2$ film, PDMS substrate was placed, and to make flawless contact between two layers, I used vacuum filtration as shown in Fig 5.2a. As a result of the process, $MoS_2$ thin film was transferred to PDMS layers with high transparency. In contrast, thicker $MoS_2$ film was transferred to PDMS substrates without vacuum filtration method (Fig. 5.2c). By using both methods, I controlled the transparency and resistivity of the $MoS_2$ thin film.

### 5.2.2 Electrical property of a $MoS_2$ thin film

The electrical property was characterized for a transferred $MoS_2$ film on a PDMS substrate by the electrical contact with the silver paste (Fig. 5.3a). Figure 5.3b shows the I-V characteristic of $MoS_2$ thin film device without any applied pressure, the resistance of the device was 200 kΩ. The electrical current was efficiently modulated by the pressure generated from a finger. When the pressure was applied to $MoS_2$ pressure sensor, the region was deformed with increasing the number of the nanosheet contacts by compression of $MoS_2$ thin films. It could improve the conductance by increasing percolating pathways of the device.

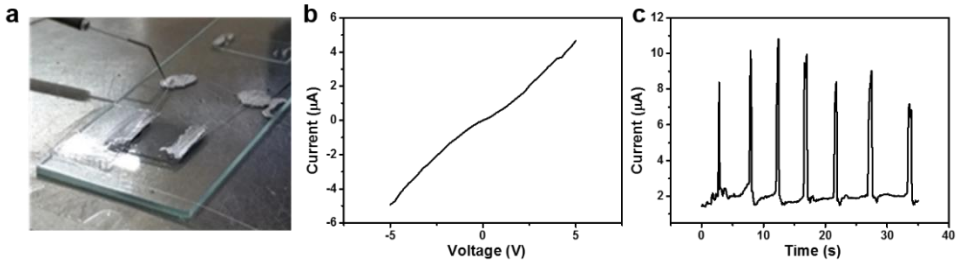


**Figure 5. 3** (a) An optical image of a $MoS_2$ thin film device. (b) I-V characteristics of a $MoS_2$ thin film device and its response from pressure (c).

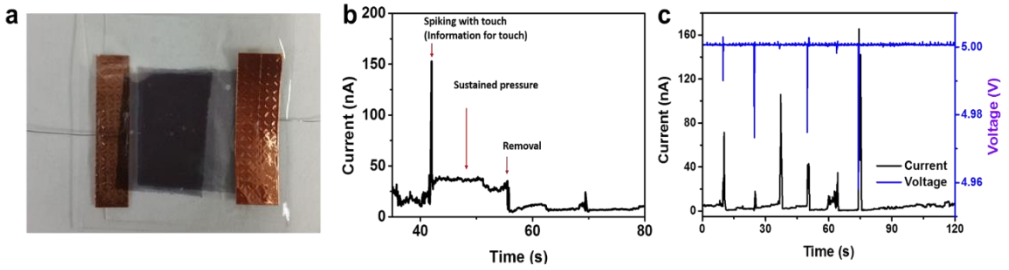


**Figure 5. 4**

### 5.2.3 Response of touch and press from a $MoS_2$ tactile sensor

To further confirm the availability of the $MoS_2$ thin film as a skin-inspired touch sensor, the thin films were integrated as a sandwiched structure by PDMS substrates as shown in Fig. 5.4a. The electrical contact was made by conductive copper tapes. Interestingly, from the electrical signals, it was possible to distinguish touch and sustained pressure in this device. Figure 5. 4b shows the electrical signal from a finger touch. When a finger touched to the surface of the device, it generates a sharp spike signal, and then the electrical conductance was maintained at a certain level during an applying pressure from the finger. In the end, the electrical signal was decreased with the removal of a finger. The sharp spike signal which is indicative to the touch could be attributed to the triboelectric effect between a fingertip and a PDMS layer. The operating mechanism was explained by coupling of contact charges between two

materials and electrostatic induction[29]. To further confirm the reason of a sharp spike signal, the current and voltage were monitored simultaneously during a finger touch on the device. With the finger touch, electrical voltage was generated at the same time at the point of the sharp spike signal (Fig. 5.4c). From the result, it is assumed that the electrical signal was generated by a voltage from the triboelectric effect between a fingertip and PDMS. Therefore, the $MoS_2$ touch sensor is available to distinguish the touch and press by triboelectric and piezoresistive effect, respectively.

## 5.3 Conclusion

In conclusion, a skin-inspired $MoS_2$ touch sensor was demonstrated with recognizing touch and press. The $MoS_2$ prepared by Li intercalation method was easily fabricated and transferred to PDMS substrates, and electrically conductive. Instant touch and sustained pressure were able to detect by a sharp spike signal and increased current originated from triboelectric and piezoresistive effect. In fact, when people grip and lift any objects, human skin provides human median nerve with distinct signals, enabling the brain to distinguish the touch and press[30]. Therefore, this result shed light on the cost-effective development for tactile sensors to handle with complex tasks.

**References:**


[1] V. J. Lumelsky , M. S. Shur , S. Wagner , *IEEE Sensors J.* **2001** , 1 , 41.

[2] D. Son *et al. Nat. Nanotechnol.* **2014**, 9, 397.

[3] J. Kim *et al. Nat. Commun.* **2014**, 5, 5747.

[4] R. S. Johansson, A. B. Vallbo. *J. Physio.,* **1979**, 286, 283-300.

[5] R. W. Vanboven, K. O. Johnson, *Neurology* **1994**, 44, 2361.

[6] R. A. Chechile. Stevens' handbook of experimental psychology vol. 4: Methodology in experimental psychology, 3rd edition. *J. Math Psychol.* **2002**, 46, 793.

[7] I. S. Riddervold *et al. Bioelectromagnetics* **2010**, 31, 380.

[8] C. Pang *et al. Nat. Mater.* **2012,** 11, 795.

[9] E. Roh, B. U. Hwang, D. Kim, B. Y. Kim, N. E. Lee. *ACS nano* **2015,** 9, 6252.

[10] D. J. Lipomi *et al*. *Chem. Mater.* **2012,** 24, 373.

[11] S. Park *et al*. *Adv. Mater.* **2014,** 26, 7324.

[12] W. Z. Wu, X. N. Wen, Z. L. Wang. *Science* **2013,** 340, 952.

[13] C. Dagdeviren *et al*. *Nat. Commun.* **2014,** 5, 4496.

[14] M. Kaltenbrunner *et al. Nature* **2013,** 499, 458.

[15] S. H. Wang *et al. Nature* **2018,** 555, 83.

[16] C. Y. Yan *et al. Adv. Mater.* **2014,** 26, 2022.

[17] C. Y. Wang, K. L. Xia, M. C. Zhang, M. Q. Jian, Y. Y. Zhang. *ACS Appl. Mater. Interfaces* **2014,** 9, 39484.

[18] J. Park *et al. ACS nano* **2014,** 8, 4689.

[19] X. W. Wang, Y. Gu, Z. P. Xiong, Z. Cui, T. Zhang. *Adv. Mater.* **2014, 26**, 1336.

[20] G. Y. Bae *et al. Adv. Mater.* **2016,** 28, 5300.

[21] Y. Pang *et al. ACS nano* **2018,** 12, 2346.

[22] S. Gong *et al. Nat. Commun.* **2014,** 5, 3132.

[23] M. J. Yin, Y. X. Zhang, Z. G. Yin, Q. D. Zheng, A. P. Zhang. *Adv. Mater. Technol.* **2018,** 3, 1800051.

[24] D. Chen, Q. B. Pei. *Chem. Rev.* **2017,** 117, 11239.

[25] S. Y. Kim *et al. Adv. Mater.* **2015,** 27, 4178.

[26] R. J. Smith *et al. Adv. Mater.* **2011,** 23, 3944.

[27] Z. Y. Zeng *et al. Angew. Chem. Int. Ed.* **2012,** 51, 9052.

[28] A. G. Kelly *et al. Science* **2017,** 356, 69.

[29] G. Zhu *et al. Nano Lett.* **2012,** 12, 4960.

[30] R. S. Johansson, J. R. Flanagan. *Nat. Rev. Neurosci.* **2009,** 10, 345.

# Chapter 6

# Discussion and Future Work

*This chapter offers a general discussion to conclude this thesis and discusses the originality of the research in this thesis. Additionally, the reconnaissance works are elaborated, which can be implemented in the future, based on researches in this thesis.*

## 6.1 General discussion

This thesis describes on the phase-controlled design and synthesis of group VI transition metal dichalcogenides, i.e., $MoS_2$ and $MoSe_2$. The physicochemical properties are characterized to confirm the different phases, and optical and electrical properties are further investigated depending on each phase. Moreover, it is studied that electrochemical property for HER on the basal plane of $MoS_2$ is dependent on different phases.

### 6.1.1 Discussion on the 1T' Phase $MoS_2$ and $MoSe_2$ Crystals

In this section, a facile method was described for the crystal phase-controlled synthesis of 1T'-$MoX_2$ (X=S, Se) crystals. The size of crystals are up to hundreds of micrometers which is enough to characterize its intrinsic properties. Based on the prepared materials, the unique properties in 1T'-$MoS_2$ were investigated such as zigzag Mo atoms structure, Raman spectrum and metallic electrical property by STEM, Raman spectroscopy and conventional electrical measurement system. Phase transition from 1T' to 2H phase was achieved by thermal annealing and laser irradiation for bulk and selected area, and it was confirmed that the materials properties were dramatically changed in different phases. Based on aforementioned findings, three different electrochemical microcell were designed to demonstrate phase-dependent HER on the basal plane of $MoS_2$.

### 6.1.2 Discussion on the skin-inspired $MoS_2$ tactile sensor

In this section, by using metallic $MoS_2$ nanosheets, I have demonstrated a skin-inspired $MoS_2$ touch sensor with recognizing touch and press. The $MoS_2$ thin films were cost-effectively fabricated by solution process such as Li intercalation and vacuum filtration method. At first, the prepared $MoS_2$ thin

film exhibited electrical conductive property with metal contacts. The electrical conductance was modulated external stimuli such as touch and press from fingertips. From the electrical signals, it was possible to investigate mechanisms to generate two shapes of signals, allowing us to recognize the moment of touch and press. Therefore, I believe this result shed light on the cost-effective development for tactile sensors to handle with complex tasks.

## 6.2 Reconnaissance work

Although some works have been reported on phase-controlled synthesis and related research in this thesis, there are opportunities to do further research in this field. Based on the current progress in this thesis, I will give a discussion on potential works.

### 6.2.1 Phase-controlled synthesis for other group VI TMDs

In chapter 4, the phase-controlled synthesis for 1T'-$MoS_2$ and $MoSe_2$ is clearly demonstrated. I think that there are two main factors for this process; the potassium molybdenum oxide, a precursor for 1T'-$MoS_2$, and flux method process. Especially, the potassium in the precursor may act as an electron donor into Mo atoms, which is similar to the phenomena from Li intercalation. Once this precursor and process are successful to prepare 1T' phase materials, it is plausible that the other group VI TMDs can be fabricated by similar precursor and process such as 1T'-$WS_2$ and $WSe_2$, because the tungsten (W) has similar d orbital state from electron configuration in the same group VI with molybdenum. Therefore, this method can be extended into other group VI TMDs for phase-controlled synthesis.

### 6.2.3 In-plane anisotropic properties of metallic 1T' Phase $MoS_2$

Among polymorphs in 2D TMDs, distorted octahedral (1T') structure has unique structure, consisting of transition metal zigzag chains, and the structure induces anisotropic properties in optical and electrical properties due to broken lattice symmetry, while most 2D TMDs show isotropic properties. For example, atomic arrangement dependent anisotropic properties have been researched for optical properties and electrical properties by $ReS_2$. Similar to anisotropy of $ReS_2$, angle-resolved magnetoresistance and Raman spectroscopy was reported in $WTe_2$ and $MoTe_2$, respectively. Therefore, metastable 1T' phase group VI transition metal dichalcogenides would be promising materials to investigate anisotropic properties.

## Publication list


[1] Y. Yu†, **G.-H. Nam**†, Q. He†, X.-J. Wu†, K. Zhang, Z. Yang, J. Chen, Q. Ma, M. Zhao, Z. Liu, F.-R. Ran, X. Wang, H. Li, X. Huang, B. Li, Q. Xiong, Q. Zhang, Z. Liu, L. Gu, Y. Du, W. Huang and H. Zhang. *Nat. Chem.* **2018**, 10, 638–643.

[2] **G.-H. Nam**, J.-H. Lee, N. E. M. Zahari, C. K. Najeeb, and J.-H. Kim. *J. Phys. Chem. C*, **2014**, *118*, 10463–10471.

[3] Z. Lai, A. Chaturvedi, Y. Wang, T. H. Tran, X. Liu, C. Tan, Z. Luo, B. Chen, Y. Huang, G.-H. Nam, Z. Zhang, Y. Chen, Z. Hu, B. Li, S. Xi, Q. Zhang, Y. Zong , L. Gu, C. Kloc, Y. Du, and H. Zhang. *J. Am. Chem. Soc.* **2018**, 140, 8563–8568

[4] J.-H. Lee, H.-K. Kwon, H.-J. Shin, **G.-H. Nam**, J.-H. Kim, and S. Choi. *ACS Appl. Mater. Interfaces*, **2018**, 10, 8417–8425.

[5] C. Tan, X. Cao, X.-J. Wu, Q. He, J. Yang, X. Zhang, J. Chen, W. Zhao, S. Han, **G.-H. Nam**, M. Sindoro, and H. Zhang. *Chem. Rev.*, **2017**, *117*, 6225–6331.

[6] R. Rajagopalan, B. Chen, Z. Zhang, X.-L. Wu, Y. Du, Y. Huang, B. Li, Y. Zong, J. Wang, **G.-H. Nam**, M. Sindoro, S. X. Dou, H. K. Liu, and H. Zhang. *Adv. Mater.* **2017**, *29*, 1605694.

[7] J.-H. Lee, C. K. Najeeb, **Gwang-Hyeon Nam**, Y. Shin, J.-H. Lim, and J.-H. Kim. *Chem. Mater.*, **2016**, *28*, 6471–6476.

[8] J.-H. Lee, Y. K. Jeong, J. A. Peters, **G.-H. Nam**, S. Jin, and J.-H. Kim. *ACS Appl. Mater. Interfaces*, **2015**, *7*, 24094–24102.